

PREPARED FOR SUBMISSION TO JCAP

Geometric and dynamic distortions in anisotropic galaxy clustering

Jonathan Blazek,^{a,b} Uroš Seljak,^{a,c,d} Zvonimir Vlah,^c and Teppei Okumura^d

^aDepartments of Physics and Astronomy, and Lawrence Berkeley National Laboratory, University of California, Berkeley, CA 94720, USA

^bCenter for Cosmology and AstroParticle Physics, The Ohio State University, Columbus, OH 43210, USA

^cInstitute of Theoretical Physics, University of Zurich, CH-8057, Zurich, Switzerland

^dInstitute for the Early Universe, Ewha University, Seoul 120-750, South Korea

E-mail: blazek@berkeley.edu

Abstract. We examine the signature of dynamic (redshift-space) distortions and geometric distortions (including the Alcock-Paczynski effect) in the context of the galaxy power spectrum measured in upcoming galaxy redshift surveys. Information comes from both the baryon acoustic oscillation (BAO) feature and the broadband power spectrum shape. Accurate modeling is required to extract this information without introducing systematic bias in the result. We consider an analytic model for the power spectrum of dark matter halos in redshift space, based on the distribution function expansion. To test the accuracy of the model, we compare with halo clustering measured in N-body simulations. We find that the distribution function model is sufficiently accurate to allow the inclusion of broadband information on scales down to $k \sim 0.2h \text{ Mpc}^{-1}$, with somewhat better accuracy for higher bias halos. Compared with a BAO-only analysis with reconstruction, including broadband shape information can improve unbiased constraints on distance measures $H(z)$ and $D_A(z)$ by $\sim 30\%$ and 20% , respectively, for a galaxy sample similar to the DESI luminous red galaxies. The gains in precision are larger in the absence of BAO reconstruction. Furthermore, including broadband shape information allows the measurement of structure growth, through redshift-space distortions. For the same galaxy sample, we find that the distribution function model is able to constrain $f\sigma_8$ to $\sim 2\%$, when simultaneously fitting for $H(z)$ and $D_A(z)$. We discuss techniques to optimize the analysis of the power spectrum, including removing modes near the line-of-sight that are particularly challenging to model, and whether these approaches can improve parameter constraints. We find that such techniques are unlikely to significantly improve constraints on geometry, although they may allow higher precision measurements of redshift-space distortions.

Keywords: galaxy clustering, redshift-space distortions, baryon acoustic oscillations

Contents

1	Introduction	1
2	Modeling galaxy clustering in redshift space	3
2.1	Clustering in real and redshift space	3
2.2	Parametrizing angular dependence	4
2.3	Geometric distortions	5
2.4	N-body simulations	7
3	The distribution function approach	7
3.1	Halo biasing	8
3.2	Stochasticity	9
3.3	Combining terms	10
3.4	Correcting higher-order angular dependence	13
4	Forecasting measurement precision and bias	16
4.1	Fisher matrix formalism	16
4.2	Separating information from the BAO feature	17
4.3	BAO damping and reconstruction	18
4.4	Optimal modeling and analysis	18
5	Forecast results	19
5.1	Constraints on geometry	20
5.2	Constraints on growth of structure	26
6	Discussion	28

1 Introduction

Galaxy redshift surveys are a primary tool in probing the universe, including the nature of dark matter and dark energy. The baryon acoustic oscillation (BAO) feature (see, e.g., [1]) can be used as a “standard ruler” to measure geometry and the expansion history of the universe. Beyond this feature, the full scale-dependence of galaxy clustering can test a number of important components of the cosmological model, including the epoch of matter-radiation equality, neutrino mass, non-Gaussianity in the initial density fluctuations, and nonlinear structure growth (e.g. [2–4]).

Galaxy redshift surveys are typically used to create a “map” in real space of the three-dimensional positions of galaxies. However, these surveys actually measure two angular coordinates and a redshift for each object, which must be converted into three-dimensional positions assuming an underlying geometry of the expanding universe. This conversion, specified by the Hubble parameter $H(z)$ and the angular-diameter distance $D_A(z)$, will introduce distortions into the resulting galaxy map if an incorrect geometry is assumed. Comparing an observed feature to a known physical scale can probe this geometry. Similarly, in an isotropic universe, clustering strength should not depend on orientation with respect to the observer. However, an anisotropic signal can arise since separations along the line-of-sight are measured

differently than those perpendicular to it. This effect is a version of the Alcock-Paczynski test [5], a method to measure the expansion of the universe using a spherically symmetric object (or feature), even without a known physical scale. The observed galaxy clustering signal will manifest these geometric distortions through both shifting of known physical scales and a warping of isotropic clustering strength. While a fully general analysis would treat these effects together, many past studies have focused on the shifting of the BAO scale, which is considered more robust to modeling uncertainties [6] but provides no constraint on growth of structure via redshift-space distortions.

Galaxies, or other objects being mapped in redshift surveys, also have peculiar velocities which contribute dynamical distortions to the observed clustering signal. The line-of-sight component of peculiar velocity contributes to the observed redshift and is thus degenerate with the cosmological redshift. This effect is commonly known as “redshift-space distortions” (RSD). RSD contain information about velocity fields and can thus provide a powerful probe of the growth of structure and potential modifications to general relativity (e.g. [7]). Indeed, measurements of RSD have the potential to be one of the primary sources of cosmological information in upcoming surveys (e.g. [8]). However, since the signatures of geometric and dynamical distortions can be quite similar, a reliable understanding of the latter is necessary to separate the two and interpret the observed clustering signal in a cosmological context. While a linear theory description of galaxy clustering in redshift space has long been available [9], significant efforts have been made in recent years to improve our analytic understanding of clustering and redshift-space distortions in the nonlinear regime (e.g. [10–17]).

Most prior attempts to constrain geometry from measurements of galaxy clustering have focused on measuring the angle-averaged BAO feature (e.g. [18–21]), which constrains a combination of distance scales approximated as $D_V(z) = D_A(z)^2/H(z)$. The greater statistical power of recent surveys has allowed the use of anisotropic clustering information from the BAO feature, the broadband clustering shape, or both to measure $D_A(z)$ and $H(z)$ separately, as well as constraining redshift-space distortions [22–28]. Current and planned redshift surveys, including BOSS,¹ eBOSS,² DESI,³ and EUCLID,⁴ offer the opportunity to probe these geometric and dynamical effects at a high level of statistical precision, requiring a thorough understanding of model uncertainties and how to extract cosmological information from the clustering signal.

Previous works have established the theoretical framework for measuring geometric and dynamical information from galaxy clustering [30–34] and have examined the constraining power and modeling requirements of such an analysis [35–40]. In this work, we discuss the information content in the full anisotropic galaxy clustering signal and compare with that in the BAO feature alone. While most previous studies focus on models of dark matter clustering, we consider the clustering of the dark matter halos in which galaxies reside. Challenges in modeling anisotropic clustering in redshift space, particularly on small scales and for separations along the line-of-sight, introduce systematic biases in cosmological parameter estimates. In light of these biases, we employ Fisher matrix formalism to determine the minimum scales that can be reliably used and discuss techniques to optimize the analysis. Several analytic models exist for galaxy clustering in redshift space. We focus in particular on the recently developed distribution function approach [12], which provides an accurate

¹Baryon Oscillation Spectroscopic Survey; <http://www.sdss3.org/surveys/boss.php>

²Extended Baryon Oscillation Spectroscopic Survey; <http://www.sdss3.org/future/eboss.php>

³Dark Energy Spectroscopic Instrument [29]

⁴<http://sci.esa.int/science-e/www/area/index.cfm?fareaid=102>

description down to comparatively small scales. While we work with the galaxy power spectrum, many recent measurements of anisotropic galaxy clustering have been done using the correlation function, for which analogous arguments apply.

This paper is organized as follows. In Section 2, we summarize the general formalism for galaxy clustering in redshift space, including the effect of geometric distortions, and describe the N-body simulations used to test analytic models. In Section 3, we describe the distribution function approach and construct a model for the full shape of the halo power spectrum in redshift space. Section 4 develops the Fisher matrix formalism used to forecast the performance of different models, and Section 5 presents the results. We conclude in Section 6 with a summary and discussion of the major results. We assume a flat, Λ CDM fiducial cosmology with $\Omega_m = 0.279$, $\Omega_b/\Omega_m = 0.165$, $h = 0.701$, $\sigma_8 = 0.807$, and $n_s = 0.96$.

2 Modeling galaxy clustering in redshift space

Numerous efforts have been made in recent years to model the clustering of galaxies in redshift space, using both N-body simulations (e.g. [15, 41]) and analytic techniques (e.g. [10, 42]). Here we summarize the relevant aspects of the field and develop a useful expansion for the geometric distortions we wish to measure.

2.1 Clustering in real and redshift space

In real space, the power spectrum, or equivalently the two-point correlation function, depends only on the amplitude of the scale being considered:

$$\langle \delta(\mathbf{k})\delta^*(\mathbf{k}') \rangle = (2\pi)^3 \delta(\mathbf{k} - \mathbf{k}') P(k), \quad (2.1)$$

where $k = |\mathbf{k}'|$. The density of a luminous tracer, such as a galaxy population, is related to that of dark matter through a biasing relationship. On large scales, a constant, linear biasing relationship is often assumed:

$$\begin{aligned} \delta_{\text{gal}} &= b_1 \delta, \\ P_{\text{gal}}(k) &= b_1^2 P_{\text{DM}}(k). \end{aligned} \quad (2.2)$$

However, this assumption breaks down on quasi-linear scales. Thus any model for galaxy clustering on small scales must consider not only the nonlinear clustering of dark matter, but also the complex bias relationship between dark matter and galaxies. In this work, we use the non-linear, non-local bias described in [43]:

$$\delta_{\text{gal}}(\mathbf{x}) = b_1 \delta(\mathbf{x}) + \frac{b_2}{2} (\delta^2(\mathbf{x}) - \langle \delta^2 \rangle) + \frac{b_s}{2} (s^2(\mathbf{x}) - \langle s^2 \rangle). \quad (2.3)$$

Non-locality comes from the tidal term $s^2(\mathbf{x}) = s_{ij}(\mathbf{x})s_{ij}(\mathbf{x})$ for tidal tensor s_{ij} :

$$s_{ij}(\mathbf{x}) = \partial_i \partial_j \Phi(\mathbf{x}) - \frac{1}{3} \delta_{ij}^{\text{K}} \delta(\mathbf{x}), \quad (2.4)$$

where δ_{ij}^{K} is the Kronecker delta function. A local, third-order bias b_3 can be trivially absorbed into the value of b_1 . The effect of a non-local third-order bias b_3^{NL} is discussed in Section 3.1.

Redshift-space distortions break the natural isotropy of Equation 2.1, leading to a dependence on the angle with respect to the line-of-sight. The observed wavevector \mathbf{k} can

be decomposed into $(k_{\parallel}, k_{\perp})$, parallel and perpendicular to the line-of-sight, respectively.⁵ Equivalently, one can use k and $\mu = \cos \theta$, where θ is the angle between \mathbf{k} and the line-of-sight:

$$\begin{aligned} k_{\parallel} &= \mu k, \\ k_{\perp} &= (1 - \mu^2)^{1/2} k. \end{aligned} \quad (2.5)$$

On large scales, in the plane-parallel approximation and with linear bias, redshift-space distortions are described by the Kaiser formula [9]:

$$P_{\text{gal}}^{\text{s}}(k, \mu) = P_{\text{DM}}^{\text{r}}(k)(b_1 + f\mu^2)^2, \quad (2.6)$$

where “s” denotes redshift space, “r” denotes real space, and the logarithmic growth rate $f = d \ln G(a) / d \ln a$, for the growth factor $G(a)$. In general relativity, $f \approx \Omega_m^{\gamma}$ with $\gamma \approx 0.55$, while theories of modified gravity can yield different values of γ [44]. Thus, a precise measurement of f via redshift-space distortions can test gravitational physics. The relationship between density and velocity fields that yield Equation 2.6 is only valid in the linear regime. Extending models of RSD to smaller scales requires a more detailed treatment of this relationship. A frequently used model is the ansatz of [10] (hereafter the “S04 model”), which includes the characteristic “fingers-of-God” (FoG) effect, in which the galaxy velocity dispersion σ_v suppresses power on small scales:

$$P_{\text{gal}}^{\text{s}}(k, \mu) = (b^2 P_{\delta\delta}(k) + 2bf\mu^2 P_{\delta\theta}(k) + f^2\mu^4 P_{\theta\theta}(k)) e^{-(f\sigma_v k \mu)^2}, \quad (2.7)$$

where $P_{\delta\delta}$, $P_{\delta\theta}$, and $P_{\theta\theta}$ are the non-linear auto- and cross-power spectra of mass density and velocity divergence.⁶

2.2 Parametrizing angular dependence

$P(k, \mu)$ must be specified on the entire two-dimensional $k - \mu$ plane (or equivalently the $k_{\parallel} - k_{\perp}$ plane). By symmetry, the auto-power spectrum in redshift space can be expanded in even powers of μ :

$$P^{\text{s}}(k, \mu) = \sum_{j=0} F_{2j}(k) \mu^{2j}. \quad (2.8)$$

This expansion should be convergent on sufficiently large scales, and the maximum j required to accurately describe the angular dependence increases with the maximum wavenumber considered, k_{max} . Similarly, it is common to express the angular dependence in terms of a multipole expansion:

$$P^{\text{s}}(k, \mu) = \sum_{j=0} A_{2j}(k) \mathcal{P}_{l=2j}(\mu), \quad (2.9)$$

where \mathcal{P}_l are the Legendre polynomials. The multipole expansion is particularly convenient from an observational perspective, since the orthogonality of the the Legendre polynomials

⁵Rotational symmetry remains on the plane perpendicular to the line-of-sight.

⁶This ansatz was originally proposed as a simple model for the redshift-space power spectrum of matter alone, but it is sometimes used, in combination with a linear bias factor, to describe galaxies.

yields a roughly diagonal covariance matrix.⁷ Measurements of the angle-averaged power spectrum include only the monopole ($l = 0$), while some recent studies (e.g. [25]) have also used the quadrupole ($l = 2$). It was shown in [36] that including terms up to the hexadecapole ($l = 4$) recovers most of the information contained in the full $P^s(k, \mu)$.

In this work, we use the full 2D clustering shape. As discussed below, we generate $P^s(k, \mu)$ using an expansion in powers of μ , truncated at μ^6 in simulations and μ^4 for analytic models. For the remainder of this work, the “s” superscript is omitted from $P(k, \mu)$, which is assumed to be in redshift space unless otherwise noted.

2.3 Geometric distortions

If the fiducial (assumed) values of the angular diameter distance, $D_A(z)$, and the Hubble parameter, $H(z)$, differ from their true values, k_{\parallel} and k_{\perp} are affected:

$$\begin{aligned} D_A(z)^{\text{true}} &= \alpha_D^{-1} D_A(z)^{\text{fid}}, \\ k_{\perp}^{\text{true}} &= \alpha_D k_{\perp}^{\text{fid}}, \\ H(z)^{\text{true}} &= \alpha_H H(z)^{\text{fid}}, \\ k_{\parallel}^{\text{true}} &= \alpha_H k_{\parallel}^{\text{fid}}, \end{aligned} \tag{2.10}$$

where the “fid” superscript indicates that the potentially incorrect fiducial cosmology has been applied. For simplicity, this superscript is dropped in the remainder of this work. One intuitive parametrization of these geometric deviations involves an isotropic “dilation”: $\alpha = (\alpha_D^2 \alpha_H)^{-1/3}$; and an anisotropic “warping”: $\epsilon = (\alpha_D / \alpha_H)^{1/3} - 1$ [31]. In the absence of redshift-space distortions (e.g. if they are removed through a reconstruction process), the position of a feature in the angle-averaged clustering signal measures α , while the angular dependence of clustering measures ϵ . We choose to use the direct α_H and α_D parametrization which is completely equivalent and may be easily applied to general clustering studies (e.g. the Lyman- α forest) where the quantities most directly measured do not correspond to α and ϵ . Note that in the presence of RSD, the quantity measured by an angle-averaged BAO measurement from galaxies can also deviate from α (e.g. [19]).

For convenience, we introduce the following small quantities:

$$\begin{aligned} \gamma_H &= \alpha_H^2 - 1 \approx 2(\alpha_H - 1), \\ \gamma_D &= 1 - \alpha_D^2 \approx 2(1 - \alpha_D). \end{aligned} \tag{2.11}$$

In terms of their fiducial values, the true wavevector amplitude and orientation are:

$$\begin{aligned} k_{\text{true}}^2 &= k^2 (1 - \gamma_D (1 - \mu^2) + \gamma_H \mu^2) \\ \mu_{\text{true}}^2 &= \mu^2 \left(\frac{1 + \gamma_H}{1 - \gamma_D (1 - \mu^2) + \gamma_H \mu^2} \right). \end{aligned} \tag{2.12}$$

In addition to assigning the observed power spectrum to incorrect values of k and μ , geometric distortions also introduce a multiplicative correction, ΔV , due to the difference in volume appearing the definition of the $P(k)$ between the true and assumed cosmologies (e.g. [30]):

$$\Delta V \equiv \left(\frac{D_A^2(z)}{H(z)} \right) \bigg/ \left(\frac{D_A^2(z)}{H(z)} \right)_{\text{true}} = \frac{D_V}{D_V^{\text{true}}} = (1 + \gamma_H)^{1/2} (1 - \gamma_D) \tag{2.13}$$

⁷The survey window function and anisotropic noise properties due to RSD can induce small off-diagonal covariance between multipoles.

Note that for the correlation function $\xi(\mathbf{r})$, which is dimensionless, the geometric distortions appear purely as rescalings of (r_\perp, r_\parallel) , and there is no additional volume correction. Together, these effects yield:

$$P_{\text{obs}}(k, \mu) = \Delta V P_{\text{true}}(k_{\text{true}}, \mu_{\text{true}}). \quad (2.14)$$

As described above, we can generically write the true angle-dependent power spectrum:

$$P_{\text{true}}(k_{\text{true}}, \mu_{\text{true}}) = \sum_{j=0} F_{2j}(k_{\text{true}}) \mu_{\text{true}}^{2j}. \quad (2.15)$$

Applying geometric distortions (i.e. Equation 2.14) to this expansion gives:

$$P_{\text{obs}}(k, \mu) = (1 + \gamma_H)^{1/2} (1 - \gamma_D) \sum_{j=0} \mu^{2j} \left(\frac{1 + \gamma_H}{1 - \gamma_D (1 - \mu^2) + \gamma_H \mu^2} \right)^j \times F_{2j} \left(k (1 - \gamma_D (1 - \mu^2) + \gamma_H \mu^2)^{1/2} \right), \quad (2.16)$$

This expression can be expanded to arbitrary order in γ_H and γ_D . When the distortions are small, the first-order expansion is sufficiently accurate:

$$\begin{aligned} P_{\text{obs}}(k, \mu) \approx & \left(\frac{1}{2} \gamma_H - \gamma_D \right) P_{\text{true}}(k, \mu) \\ & + \mu^0 \left[F_0^{(0)} - (k^2 \gamma_D) F_0^{(1)} \right] \\ & + \mu^2 \left[(1 + \gamma_D + \gamma_H) F_1^{(0)} + k^2 (\gamma_D + \gamma_H) F_0^{(1)} - (k^2 \gamma_D) F_1^{(1)} \right] \\ & + \mu^4 \left[(1 + 2\gamma_D + 2\gamma_H) F_2^{(0)} - (\gamma_D + \gamma_H) F_1^{(0)} + k^2 (\gamma_D + \gamma_H) F_1^{(1)} - (k^2 \gamma_D) F_2^{(1)} \right] \\ & + \mu^6 \left[(1 + 3\gamma_D + 3\gamma_H) F_3^{(0)} - 2(\gamma_D + \gamma_H) F_2^{(0)} + k^2 (\gamma_D + \gamma_H) F_2^{(1)} - (k^2 \gamma_D) F_3^{(1)} \right] \\ & + \dots, \end{aligned} \quad (2.17)$$

where $F_j^{(n)} \equiv (\partial/\partial k^2)^n F_j$, and terms scaling as μ^8 and above aren't shown. The first line of the equality shows the overall amplitude shift due to the fractional change in volume, ΔV . We use this expansion to include geometric distortions in the Fisher matrix formalism described below.

The shift of clustering power from lower to higher powers of μ is one signature of these geometric distortions. For instance, the Kaiser formula predicts zero power at μ^6 and above (or the equivalent multipoles). In principle, measuring this angular dependence on large scales (where linear theory holds) would be a clean detection channel for geometric distortions. There are significantly more modes on small scales (high k), providing the possibility of much higher signal-to-noise, although using these smaller scales requires understanding nonlinear effects. Accurate modeling of nonlinear clustering and redshift-space distortions helps extract information in two ways. First, the broadband and BAO features in the power spectrum provide specific distance scales that can be used as standard rulers. Second, an understanding of how redshift-space distortions induce anisotropy in the power spectrum is required to perform an Alcock-Paczynski test.

2.4 N-body simulations

We use the clustering of dark matter halos in N-body simulations as a reference against which to compare different models. Since galaxies reside in dark matter halos, N-body simulations provide an important link in understanding observed clustering and redshift-space distortions. However, the physics of galaxy formation and existence of satellite galaxies can lead to a non-trivial relationship between halos and galaxies (e.g. [45]). We consider the clustering of dark matter halos and leave the halo-galaxy relationship for future work (see, e.g., [46] for a recent exploration of this relationship in the context of galaxy clustering). The modeling of central galaxies, which should exhibit clustering properties similar to halos, is more straightforward. Some galaxy types used in clustering measurements, e.g. luminous red galaxies (LRGs), are primarily central objects, and it may be possible to construct a sample with a low level of satellite contamination [45].

The power spectra in the distribution function expansion, described in Section 3, are from mass-weighted velocity moments and are thus straightforward to determine from simulations, since the contribution from empty grid cells is well-defined. We use results calculated from N -body simulations as described in [15, 16]. We provide a brief summary of these simulations here.

We employ a series of N -body simulations of the Λ CDM cosmology seeded with Gaussian initial conditions, an updated version of [47]. The fiducial cosmology corresponds to the best-fit parameters in the WMAP 5-year data [48], with $\Omega_m = 0.279$, $\Omega_b = 0.0462$, $h = 0.701$, $n_s = 0.96$, and a normalization of the curvature perturbations corresponding to a density fluctuation amplitude $\sigma_8 = 0.807$. A total of 1024^3 particles of mass $m_p = 2.95 \times 10^{11} h^{-1} M_\odot$ are placed in a cubic box with side length $1600h \text{ Mpc}^{-1}$. To reduce sample variance, 12 simulations are used and each of the three lines-of-sight are treated as independent for 36 total realizations.

Dark matter halos are identified at the four redshifts using the friends-of-friends algorithm [49] with a linking length equal to 0.17 times the mean particle separation. Halos must have at least 20 particles and are divided into subsamples by mass. Properties of the constructed halo catalogs at $z = 0$ and 0.509 (quoted as $z = 0.5$) are summarized in Table 1. In most of this work, we focus on the two lowest halo mass bins at $z = 0.5$.

In [15], these simulations were analyzed to extract the velocity moment power spectra for halos (see Section 3). To obtain $P(k, \mu)$ for model comparison, we sum these terms following the distribution function expansion to include all contributions up to μ^6 . This provides greater resolution in μ than using $P(k, \mu)$ directly calculated in redshift space. Figure 1 compares $P(k, \mu)$ constructed with these two approaches, with the shot noise removed. They are in reasonable agreement, when compared with the expected measurement uncertainty, indicating that we can neglect higher powers of μ for $k \lesssim 0.3h \text{ Mpc}^{-1}$.

3 The distribution function approach

The recently developed distribution function (DF) approach to redshift-space distortions expands the density field in redshift-space in terms of moments of the distribution function [12]. The resulting redshift-space power spectrum is expressed in terms of real-space correlations between mass-weighted powers of the velocity field:

$$P^s(\mathbf{k}) = \sum_{L=0}^{\infty} \sum_{L'=0}^{\infty} \frac{(-1)^{L'}}{L!L'!} \left(\frac{ik\mu}{\mathcal{H}} \right)^{L+L'} P_{LL'}^r(\mathbf{k}), \quad (3.1)$$

z	Mass bin	Mass range ($10^{12}h^{-1}M_{\odot}$)	\bar{N} ($\times 10^4$)	\bar{n} ($h^3\text{Mpc}^{-3}$)	b_1 (cross)	$b_{2,00}$	$b_{2,01}$
0	1	5.91 – 17.7	175	4.28×10^{-4}	1.18	-0.39	-0.45
	2	17.7 – 53.2	63.3	1.54×10^{-4}	1.47	-0.08	-0.35
	3	53.2 – 159	18.7	4.57×10^{-5}	2.04	0.91	0.14
	4	159 – 467	4.05	9.89×10^{-6}	3.05	3.88	2.0
0.5	1	5.91 – 17.7	144	3.51×10^{-4}	1.64	0.18	-0.20
	2	17.7 – 53.2	44.8	1.09×10^{-4}	2.18	1.29	0.48
	3	53.2 – 159	9.96	2.43×10^{-5}	3.13	4.48	2.6
	4	159 – 467	1.30	3.18×10^{-6}	4.82	12.65	9.5

Table 1. Properties of halo catalogs. \bar{N} and \bar{n} are the average number and number density of halos in each realization, respectively. The linear bias values b_1 are computed from the cross power spectrum (P_{00}^{mh}), averaged at $0.01 \leq k \leq 0.04h\text{Mpc}^{-1}$. The quadratic bias values b_2^{00} and b_2^{01} are fit to P_{00} and P_{01} , respectively, as in [14]. The b_2 values shown here are fit after applying a correction to the relevant perturbation theory terms, as discussed in Section 3.3. Fitting without this correction yields different b_2 values.

where $\mathcal{H} = aH$, and $P_{LL'}^r$ is the real-space power spectrum of density weighted powers L and L' of the radial velocity field. For instance, P_{00} is the standard density auto-power spectrum, while P_{01} is the cross-power spectrum of density and radial momentum.

This approach naturally produces an expansion of $P(k, \mu)$ in powers of μ , which is convergent on sufficiently large scales, with a finite number of correlations contributing at a given power of μ . Thus, when considering geometric distortions, we use an expansion in powers of μ rather than multipoles, which have contributions from all higher powers of μ and thus, in principle, an infinite number of correlations between distribution function moments.

This expansion is valid for the density field of both dark matter and biased tracers of dark matter such as halos or galaxies. The $P_{LL'}$ terms have recently been explored in simulations [15, 16] and calculated perturbatively [13, 14]. In this work, we are interested in using the distribution function expansion to provide a more accurate model that can be fit to observations of clustering in redshift-space. While N-body simulations can provide such a model for halos directly, spanning the necessary cosmological parameter space is not feasible.⁸ Instead, we seek an analytic (or hybrid) approach that allows the rapid calculation of the redshift-space clustering for a given cosmology.

3.1 Halo biasing

For dark matter, such an analytic approach involves calculating the relevant terms perturbatively to the desired order. Halo clustering, however, requires additional parameters to account for the unknown relationship between biased tracers and the underlying density field. We employ a non-linear and non-local biasing model [43], resulting in four bias parameters for each redshift and halo mass bin: $\{b_1, b_2^{00}, b_2^{01}, b_s\}$, where P_{00} and P_{01} have different values for quadratic, local bias b_2 (see [14] for further discussion). Although it is not included in this parametrization, the contribution from a non-local third-order bias, b_3^{NL} [51], remains significant and is responsible for the two different values of b_2 . We would have obtained similar results with a bias parametrization using $\{b_1, b_2, b_3^{\text{NL}}, b_s\}$. While the

⁸Recent work on simulation-based cosmic emulators, e.g. [50], may provide an alternative approach.

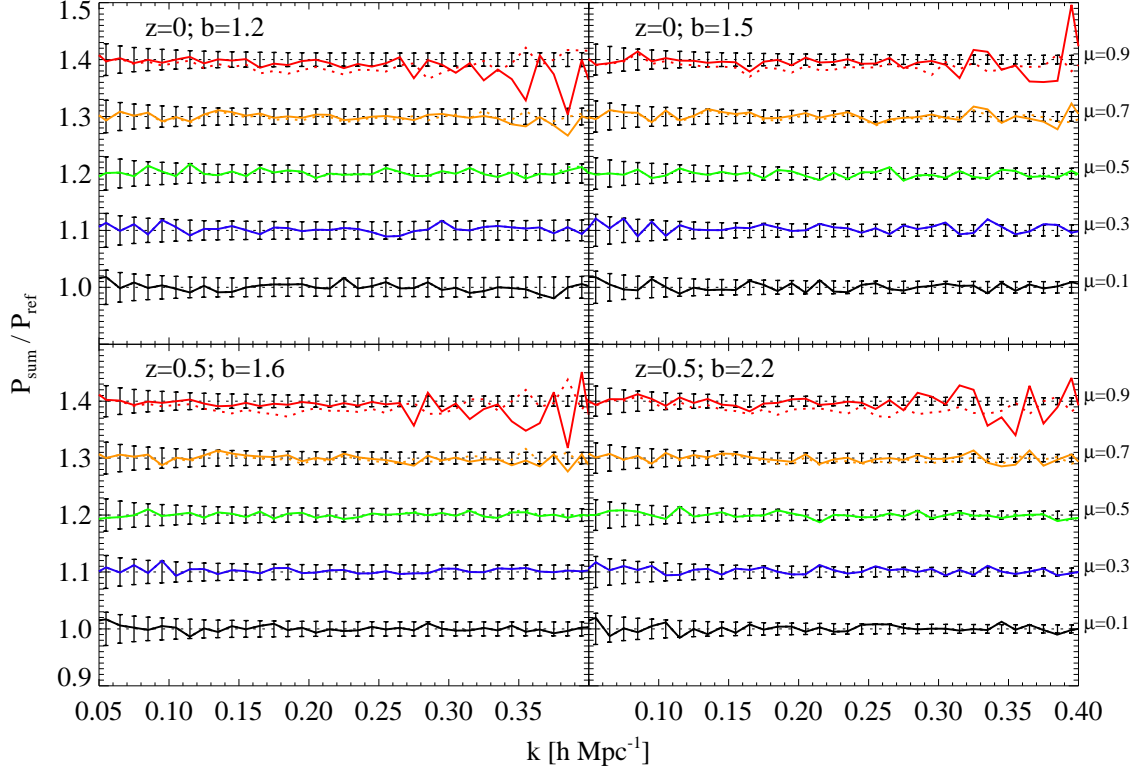


Figure 1. $P(k, \mu)$ calculated by summing over μ^{2j} terms is shown, normalized by the reference $P(k, \mu)$ calculated directly from simulations. The full scale-dependent shot noise $\Lambda(k)$ is subtracted from both the reference and summed $P(k, \mu)$; see Equation 3.2. *Left panels* show the lowest halo mass bin, and *right panels* show the second mass bin; $z = 0$ (*top panels*) and $z = 0.5$ (*bottom panels*). See Table 1 for more information on halo mass and bias. Five evenly spaced angular bins for $0 < \mu < 1$ are shown, with vertical offsets added to increasing μ values. Error bars show the expected (fractional) uncertainty for a survey similar to the DESI LRGs (see Section 5). Solid lines show the sum of distribution function terms, calculated from the simulations, up to μ^6 . Dotted lines, only distinguishable at higher values of μ , show the sum up to μ^4 .

nonlinear bias values could each be treated as an independent parameter, doing so would ignore theoretical understanding of the relationship between them (e.g. [43, 52]) and would reduce the constraining power of the observations. Instead, we treat them as functions of the linear bias b_1 , yielding one redshift-dependent bias parameter for each halo mass bin. To leading order, $b_s = (2/7)(1 - b_1)$. The b_2 parameters have an approximately quadratic dependence on b_1 , which is fit to the simulations. The model also contains a halo velocity dispersion σ_v . The linear theory prediction of this term (e.g. [14]) is sufficiently accurate for the model: $\sigma_v \approx \sigma_{v,\text{lin}} \sim f(z)D(z)$. Thus the velocity dispersion contributes no additional free parameters.

3.2 Stochasticity

A further complication to modeling the clustering of halos is their stochastic nature as a tracer of the density field. This contribution is commonly modeled as a Poissonian shot

noise: $P_{\text{shot}} = 1/\bar{n}$, for average number density \bar{n} . However scale-dependent corrections due to halo exclusion and non-linear clustering can be significant [53]. Although our Fisher forecast assumes Poissonian shot noise when assessing the information content of the power spectrum, we must account for deviations from this simple assumption when comparing the clustering of halos in simulations (which has non-Poissonian shot noise) to the distribution function model.

Significant progress has been made in understanding these non-Poissonian contributions (e.g. [53]). However, a complete and reliable model does not yet exist. Instead, the full stochastic term, $\Lambda(k)$, can be estimated following the approach of [54]:

$$\Lambda(k) = P_{00}^{\text{hh}}(k) - 2b_1 P_{00}^{\text{hm}}(k) + b_1^2 P_{00}^{\text{mm}}(k), \quad (3.2)$$

where “h” and “m” refer to halos and matter, respectively, and correlations are calculated in real space. The most conservative treatment of shot noise would allow for marginalization over a multi-parameter model able to capture the relevant scale-dependence (e.g. Equation 2.23 of [14]). Such an approach would suppress information on small scales, where shot noise dominates. Conversely, a reliable model for shot noise would provide information on halo or galaxy properties from the additional scale-dependence. In this work, we take an intermediate approach. We assume that the non-Poissonian corrections are understood such that no additional marginalization is required. However, when performing forecasts, these terms are left out of the derivatives with respect to the parameters of interest (i.e. the shot noise correction contributes no information).

3.3 Combining terms

For simplicity, we choose to consider terms in the DF expansion (Equation 3.1) up to μ^4 . Although including higher μ terms would improve the model accuracy at $\mu \approx 1$, as seen in Figure 1, these terms on the scales of interest tend to be smaller than the expected survey measurement uncertainty. Moreover, higher powers of μ have contributions from an increasing number of $P_{LL'}$ correlations and are thus more computationally intensive. Instead, as discussed in Section 3.4, we apply a correction, a_4 , to the μ^4 term. We write the halo power spectrum in redshift space:

$$P^{\text{hh}}(k, \mu) = A(k) + B(k)\mu^2 + (1 + a_4 k^2)C(k)\mu^4, \quad (3.3)$$

where the k -dependent terms are determined by summing the relevant components of the real-space $P_{LL'}^{\text{hh}}$ correlations:

$$\begin{aligned} A(k) &= P_{00, \mu^0}^{\text{hh}}(k), \\ B(k) &= P_{01, \mu^2}^{\text{hh}}(k) + P_{02, \mu^2}^{\text{hh}}(k) + P_{11, \mu^2}^{\text{hh}}(k), \\ C(k) &= P_{11, \mu^4}^{\text{hh}}(k) + P_{02, \mu^4}^{\text{hh}}(k) + P_{12, \mu^4}^{\text{hh}}(k) + P_{03, \mu^4}^{\text{hh}}(k) + P_{13, \mu^4}^{\text{hh}}(k) + P_{22, \mu^4}^{\text{hh}}(k) + P_{04, \mu^4}^{\text{hh}}(k). \end{aligned} \quad (3.4)$$

The DF model terms are calculated analytically by applying the nonlinear biasing model to the relevant $P_{LL'}^{\text{hh}}$ terms calculated with Eulerian perturbation theory (PT) [14]. However, the accuracy of the PT calculations can break down on comparatively large scales. While recent and ongoing work has made large improvements in perturbative techniques (e.g. [55–57]), we seek here to test the distribution function expansion mapping from real to redshift space and the nonlinear biasing scheme, rather than the accuracy of a particular perturbation theory approach. For a few of the dominant terms in the model, where accurate PT

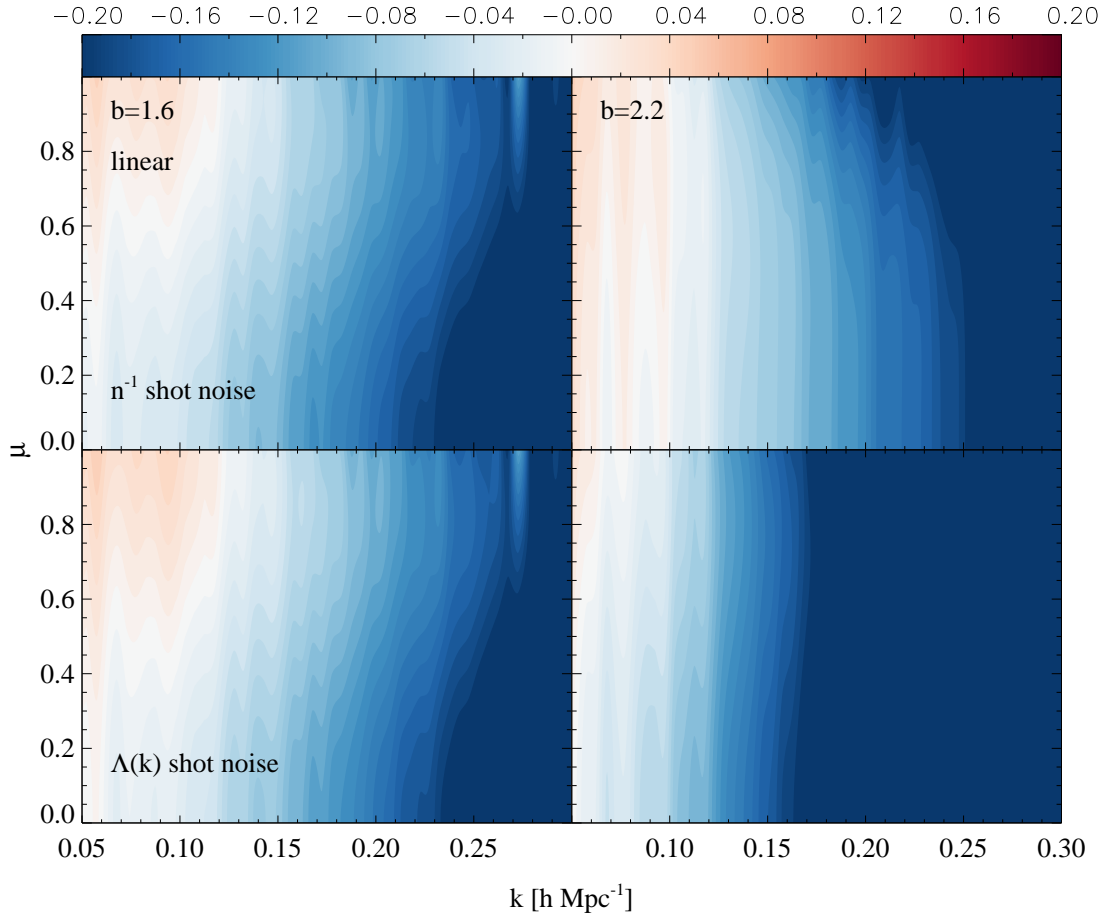


Figure 2. The fractional difference $(P_{\text{model}}/P_{\text{sim}} - 1)$ between the linear Kaiser model and simulations is shown at $z = 0.5$, for halos with $b_1 = 1.6$ (left panels) and $b_1 = 2.2$ (right panels). *Top panels:* Simulations have been corrected assuming the standard Poissonian shot noise. *Bottom panels:* The full k -dependent shot noise is used (as discussed in Section 3.2). The non-Poissonian correction is more significant for higher bias halos. Note that fractional differences greater than ± 0.20 are truncated at that value.

predictions are particularly challenging - namely the scalar parts of P_{00}^{mm} , P_{01}^{mm} , and P_{11}^{mm} - we apply a scale-dependent correction factor to the PT terms to bring them into agreement with the dark matter results from N-body simulations. This correction is applied before determining the best-fit bias values. The effect of this correction is seen in Figure 6. Taken together, the assumptions made about our ability to model nonlinear dark matter clustering, bias, and shot noise are somewhat optimistic. As such, the statistical power of this model demonstrates the gains that come with recent and (hopefully) future improvements in understanding these processes. Once the shape of the linear power spectrum is fixed, the model can be expressed with the following parameters: $\{f(z), \sigma_8(z), b_1(z), a_4(z)\}$, in addition to the geometric distortions discussed in Section 2.3. The parameter $\sigma_8(z)$ refers here to the

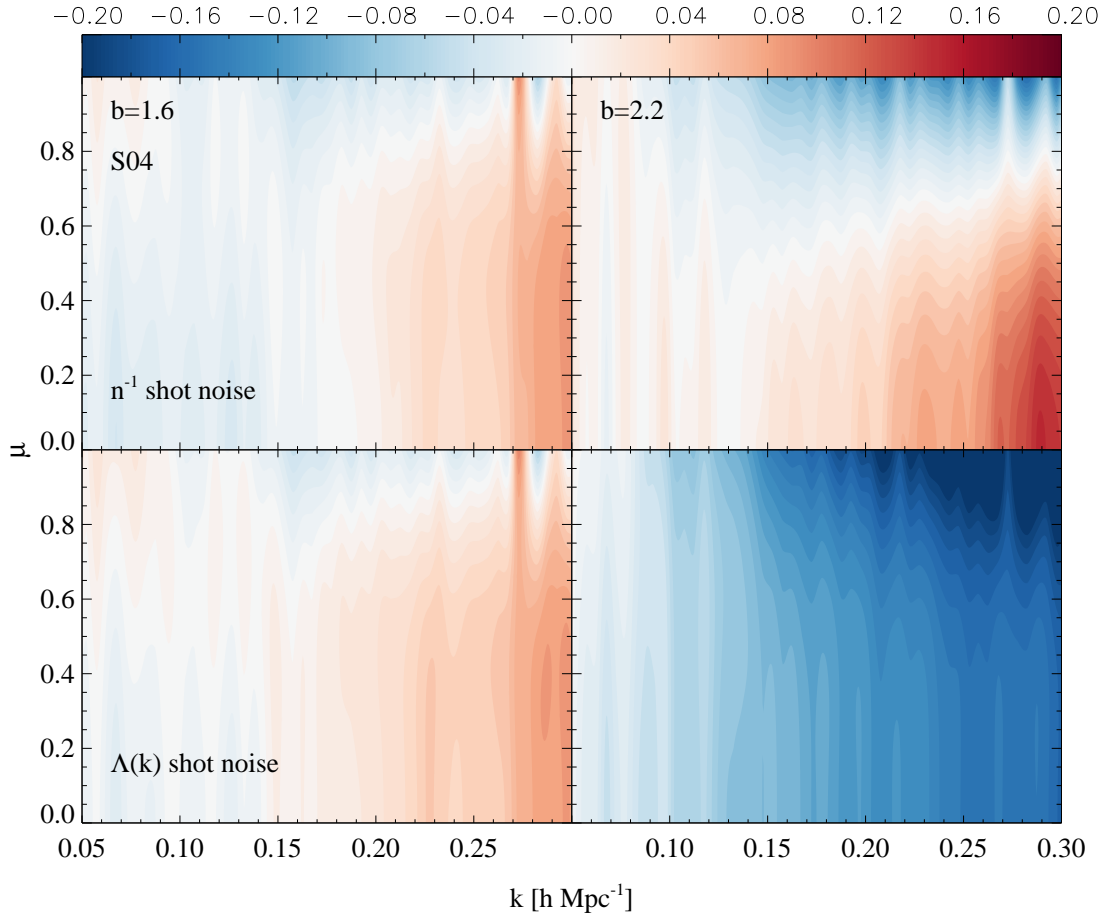


Figure 3. The S04 model is compared to simulations, with the same conventions as Figure 2.

amplitude of the linear matter power spectrum at redshift z .

Figures 2-6 show the accuracy of the DF model, as well as the linear Kaiser model and the S04 model with no FoG (since the velocity dispersion for halos is small). Figure 2 compares the Kaiser model with the simulation results for both Poissonian and scale-dependent shot noise. Figures 3 and 4 show the same for the S04 and DF models, respectively. Figure 5 shows the accuracy of the DF model compared to the measurement precision of $P(k, \mu)$ expected from a survey similar to the DESI LRGs, while Figure 6 compares different versions of the DF model, including the μ^4 correction discussed in Section 3.4, with simulation results. In these comparisons, shot noise is subtracted from the simulation results rather than added to the model. This choice is somewhat arbitrary - the scale-dependent contribution could alternatively be considered part of the bias model. However, this convention matches the form of the Fisher matrix calculation, where shot noise is assumed to be Poissonian. Note the apparent accuracy of the S04 model when standard Poissonian shot noise is applied. Although it is a less sophisticated model, chance cancellations of neglected effects yield sur-

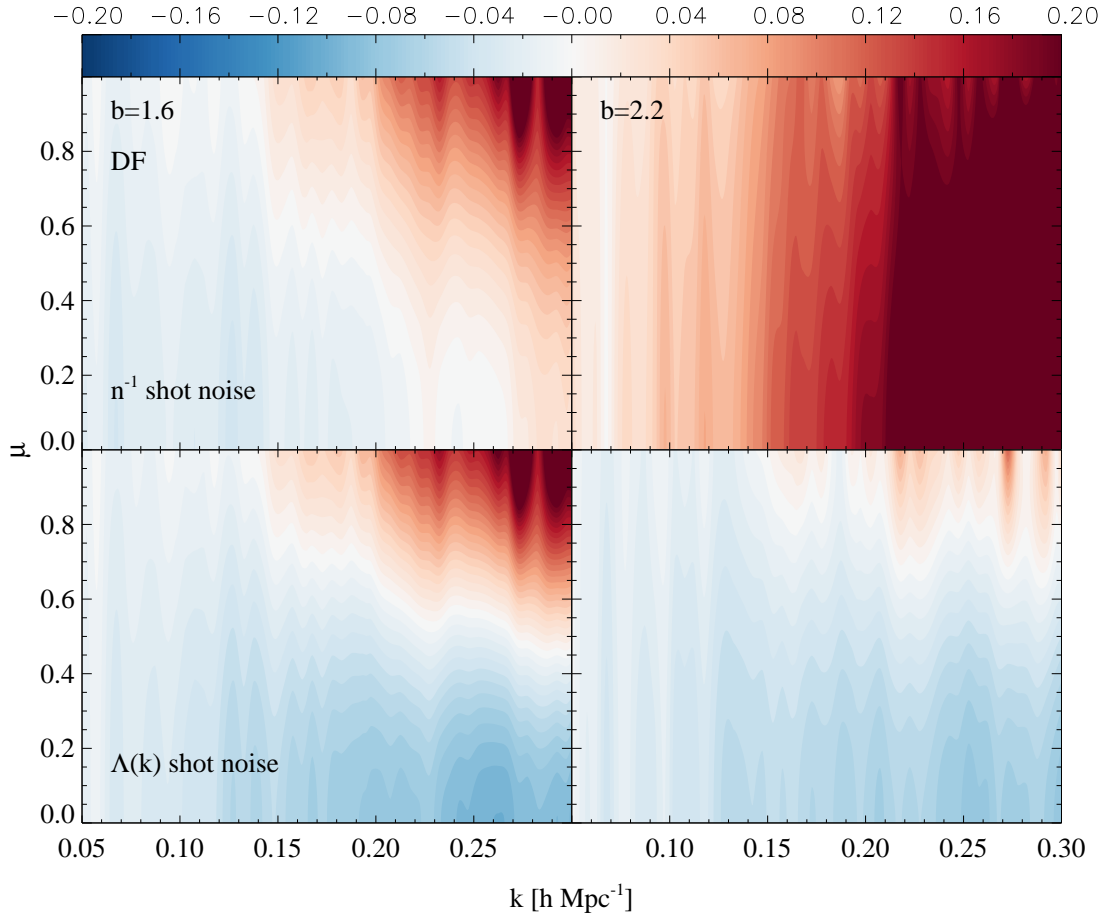


Figure 4. The DF model is compared to simulations, with the same conventions as Figure 2. The model includes the PT correction (see Section 3.3) and has $a_4 = 0$ (see Equation 3.3).

prising agreement with the simulations, particularly for $b_1 = 1.6$ halos. Apparent features on the largest scales in these figures are due to scatter in the simulation measurements.

3.4 Correcting higher-order angular dependence

The distribution function model in Equations 3.3-3.4 is complete up to terms scaling as μ^4 . Higher angular terms quickly become significant on small scales, and the model must thus include these terms for large values of $k_{\parallel} = k\mu$. In addition to these higher μ terms, the model prediction for the μ^4 term itself diverges from the simulation results at high k , primarily due to a breakdown in the biasing model [14].

One or more free parameters can improve the model accuracy on small scales. Although additional free parameters must be constrained from the observations, at the cost of statistical power, in principle the increased accuracy can allow the extraction of information on smaller scales, where the number of modes rapidly increases. It is thus worth exploring whether such an approach improves constraints on the parameters of interest.

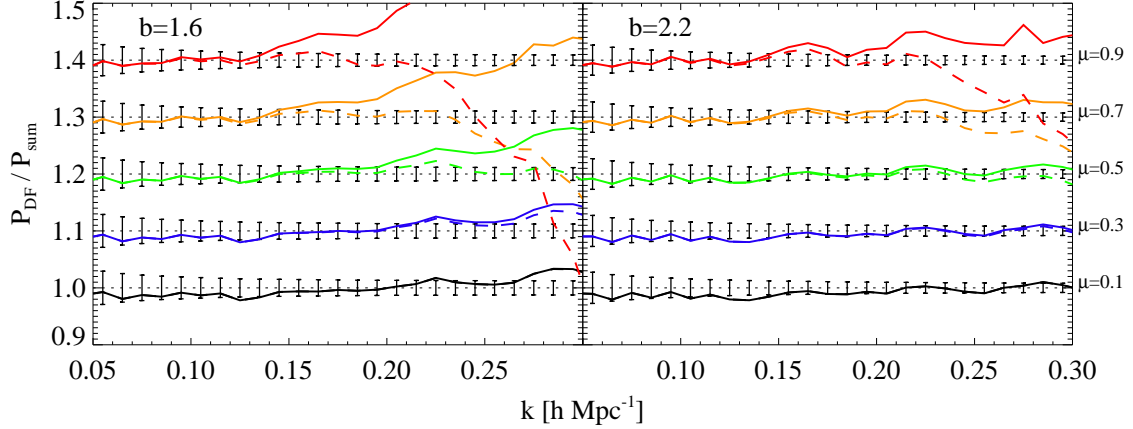


Figure 5. The fractional difference between the distribution function model and the simulation $P(k, \mu)$ is shown for halos with bias 1.6 and 2.2 at $z = 0.5$. Solid lines show the DF model with $a_4 = 0$. Dashed lines use the best-fit a_4 value, as discussed in Section 3.4. Five evenly spaced angular bins for $0 < \mu < 1$ are shown, with vertical offsets added to increasing μ values. Comparison is made with the summed $P(k, \mu)$ calculated using terms up to μ^6 . Error bars show the expected (fractional) uncertainty for a survey similar to the DESI LRGs. The k -dependent stochasticity correction is applied to simulation results, and the PT correction is included in the DF model.

We choose the correction: $F_4(k)\mu^4 \rightarrow (1 + a_4 k^4)F_4(k)\mu^4$, which depends on $k_{\parallel} = k\mu$, as would appear in an FoG expansion. However, this choice is somewhat arbitrary, and other reasonable corrections could be applied. The a_4 parameter partially accounts for deviations between the μ^4 term in simulations and calculated analytically, as well as the missing higher μ terms, although the latter effect is sub-dominant on scales of interest. The value of a_4 becomes an additional free parameter that must be determined from the data, with a fiducial value determined using χ^2 minimization with respect to the simulation results, weighting by the number of modes and signal-to-noise in each \mathbf{k} -bin (ignoring shot noise), up to $k = 0.2h \text{ Mpc}^{-1}$. This choice was made to prevent smaller scales that are unlikely to be used in cosmological analyses from dominating the fit. Figures 5 and 6 demonstrate the effect of this correction term. We compare the resulting parameter constraints with and without this correction below. Note that geometric distortions of this correction term are ignored when taking derivatives for the Fisher matrix below. Although the correction affects the amplitude of the underlying power spectrum, its particular form should not contribute any cosmological information.

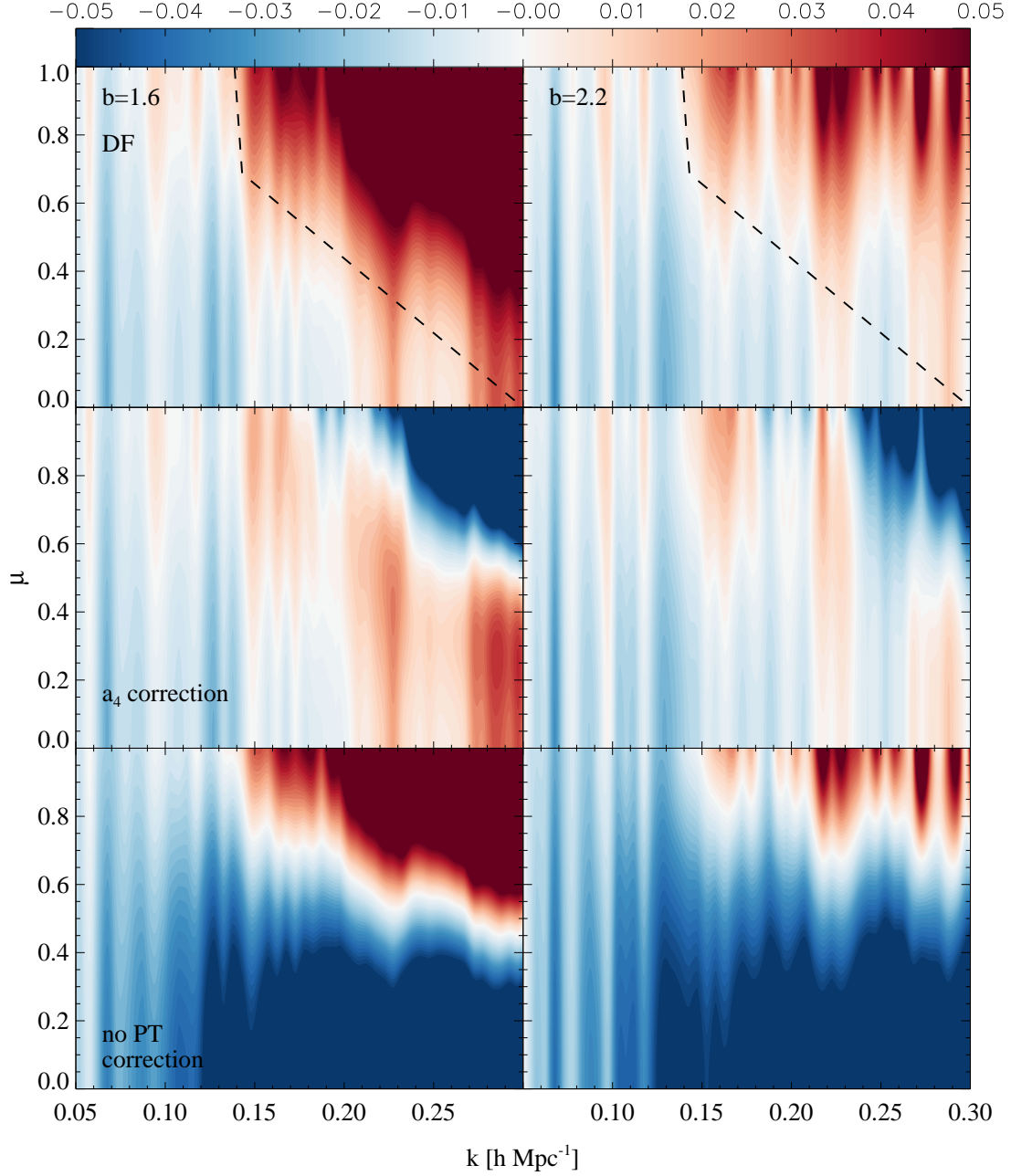


Figure 6. The fractional difference between the distribution function model and simulations is shown at $z = 0.5$. In all cases, the full k -dependent shot noise is used. *Top panels:* The DF model with $a_4 = 0$ and with the PT correction discussed in Section 3.3; *middle panels:* the DF model with the PT correction and best-fit a_4 correction (Equation 3.3); *bottom panels:* the DF model with $a_4 = 0$ and without the PT correction. The dashed line indicates a μ -dependent cut in k that could increase the unbiased signal for parameter estimation, as discussed in Section 4.4. Note that the fractional difference is truncated at $\pm 5\%$ instead of $\pm 20\%$ as done in Figures 2-4.

4 Forecasting measurement precision and bias

We wish to determine how well a galaxy redshift survey can constrain cosmological physics by measuring geometric distortions (D_A and H) and dynamical distortions (f or $f\sigma_8$). The achieved precision and accuracy depend on the underlying model for clustering in redshift space. Attempting to use measurements on small scales where the model breaks down will introduce a systematic bias to parameter estimates, even while reducing the statistical errors. In general, a more complicated model (with additional free parameters) will reduce this systematic bias at the cost of statistical constraining power.

We employ the Fisher matrix formalism to forecast parameter constraints around a fiducial cosmology. We assume a fixed shape for the linear power spectrum (a reasonable approximation, given the precision from Planck measurements), and only allow the following parameters (or a subset thereof) to vary: $\{H, D_A, f, \sigma_8, b_1, a_4\}$. As discussed in [24], relaxing a hard prior on the linear power spectrum shape has no discernible effect on the ultimate constraints on H , D_A , and f . In general, however, it is important to note that the BAO feature constrains D_A/r_s and Hr_s , for sound horizon r_s . The quantities constrained with broadband features will depend on the cosmological parameters that determine their shape and scale, while the AP and volume effects directly measure combinations of D_A and H . A more complete analysis including changes in the underlying cosmological parameters would consistently account for these dependencies. The growth factor, $G(z)$, is completely degenerate with σ_8 , and it is thus not considered as a separate parameter. For linear theory, there are only two independent combinations of the set $\{b_1, f, \sigma_8\}$, namely $\{b_1\sigma_8, f\sigma_8\}$. However, the distribution function model depends on all three independently, as discussed below.

4.1 Fisher matrix formalism

The amount of information about the parameters p_i , contained by a set of observables with covariance matrix C , is given by the Fisher matrix:

$$F_{ij} = \frac{1}{2} \text{Tr} [C_{,i} C^{-1} C_{,j} C^{-1}], \quad (4.1)$$

where $C_{,i} \equiv \partial C / \partial p_i$. For the two-dimensional redshift-space power spectrum $P(k, \mu)$, measured in a galaxy survey, the Fisher matrix can be written [58, 59]:

$$F_{ij} = \int_{k_{\min}}^{k_{\max}} \frac{2\pi k^2 dk}{(2\pi)^3} \int_0^1 d\mu \left(\frac{\partial \ln P(k, \mu)}{\partial p_i} \right) \left(\frac{\partial \ln P(k, \mu)}{\partial p_j} \right) V_{\text{eff}}(k, \mu), \quad (4.2)$$

where the effective volume determines the signal-to-noise in $P(k, \mu)$:

$$V_{\text{eff}} = V_s \left[\frac{\bar{n} P(k, \mu)}{1 + \bar{n} P(k, \mu)} \right]^2, \quad (4.3)$$

for survey parameters V_s (volume) and \bar{n} (galaxy number density). Equation 4.2 assumes that the power spectrum measurements for each mode \mathbf{k} are independent, with uncertainty given by $\sigma_P/P \propto V_{\text{eff}}^{-1/2}$, which includes both sample variance and Poissonian shot noise \bar{n}^{-1} . On sufficiently small scales, this formula breaks down as power spectrum measurements on different scales become correlated. For a given measurement, the Fisher matrix provides the minimum marginalized statistical uncertainty on p_i : $\sigma_i = (F_{ii}^{-1})^{1/2}$. Independent measurements can be combined by adding their respective Fisher matrices.

This formalism can also be used to estimate the systematic bias on p_i that comes from assuming an incorrect model, denoted P' , instead of the true P . Following [36], the bias on p_i is given by:

$$\Delta p_i = - \sum_j (F'_{ij})^{-1} s_j, \quad (4.4)$$

$$s_j = \int_{k_{\min}}^{k_{\max}} \frac{2\pi k^2 dk}{(2\pi)^3} \int_0^1 d\mu \left(\frac{P'(k, \mu) - P(k, \mu)}{P'(k, \mu)} \right) \left(\frac{\partial \ln P'(k, \mu)}{\partial p_j} \right) V'_{\text{eff}}(k, \mu),$$

where F'_{ij} and V'_{eff} are calculated using P' . This expression is derived by expanding around the maximum of the likelihood and is thus only valid when the parameter bias (i.e. the shift away from the maximum) is small. However, we are only concerned with the case $\Delta p_i \lesssim \sigma_i$, where Equation 4.4 remains applicable. Beyond this point, the parameter estimate has been biased beyond the level of the statistical uncertainty and is unreliable. As seen below, a parameter estimate can quickly become biased as information from smaller scales is included. The number of modes rapidly increases (driving down the statistical errors), while simultaneously the modeling of nonlinear clustering, redshift-space distortions, and biasing becomes inaccurate.

To model the “true” $P(k, \mu)$, we use the halo measurements from N-body simulations. Although we assume simple Poissonian shot noise in the Fisher calculation, the true shot noise is somewhat non-Poissonian and k -dependent (as discussed in Section 3.2). We subtract this corrected shot noise from the simulation $P(k, \mu)$.

Recently, [8] parameterized the loss of information on small scales due to nonlinear evolution by applying an overall suppression to the linear theory information, with a suppression factor equivalent to that in Equation 4.5. Instead, our approach directly measures the information content in the nonlinear model and uses the systematic bias to indicate where this information is no longer reliable. In addition to applying a k_{\max} , determined by the systematic bias, we could relax some of the (optimistic) assumptions made in constructing the DF model, leading to additional free parameters that would serve to decrease the information content.

4.2 Separating information from the BAO feature

We wish to isolate information coming from the BAO feature, which provides a known physical scale, and the broadband shape, which lacks sharp features. We model the power spectrum as $P = P_{\text{BAO}} + P_{\text{BB}}$ and separate these components with a basis spline, which fits the smooth broadband shape of the power spectrum. This technique is similar to that employed in [19]. We mitigate the challenge of fitting the rapidly changing power spectrum by first dividing by the baryon-free approximation of [1]. For the linear power spectrum, where both an analytic approximation and a basis spline model for P_{BB} are available, we find no appreciable difference in BAO information content in the two approaches. We note the importance of high resolution input power spectra to model the BAO information. If the power spectrum is sampled at insufficient resolution, the amplitude of numerical derivatives of the BAO feature is reduced, leading to a spurious reduction in the forecast sensitivity to parameters.

In the following sections, where results are shown for individual values of k_{\max} , all BAO information is included, and k_{\max} refers to the broadband information only.⁹ Where

⁹In this work, “all BAO information” means that $k_{\max}^{\text{BAO}} = 0.4 \, h \, \text{Mpc}^{-1}$, a somewhat arbitrary choice that has no impact on the results, given the BAO damping.

results are shown as a continuous function of k_{max} , BAO and broadband information are both truncated at k_{max} .

4.3 BAO damping and reconstruction

Nonlinear evolution damps the BAO feature on small scales. These effects are automatically included in the nonlinear treatment of the distribution function model. For linear theory, we use the formalism of [6, 60] to account for the loss of information due to this damping:

$$P_{\text{BAO,NL}}(k, \mu) = P_{\text{BAO,lin}}(k, \mu) \exp \left[-\frac{1}{2} k^2 \Sigma^2 ((1 - \mu^2) + (1 + f)^2 \mu^2) \right], \quad (4.5)$$

$$\Sigma(z) \approx 9.4 \left(\frac{\sigma_8(z=0)}{0.9} \right) \left(\frac{D(z)}{D(z=0)} \right) h^{-1} \text{Mpc},$$

where $\Sigma(z)$ is the rms Lagrangian displacement, which is enhanced (in redshift space) along the line-of-sight by RSD, yielding the factor of $(1 + f)$. Reconstruction of the density field [61] partially restores this information by removing some of the nonlinear displacements of density tracers. In the framework of Fisher forecasts, reconstruction effectively reduces Σ . “Standard” reconstruction assumes $\Sigma \rightarrow \Sigma/2$.

To include BAO reconstruction with the DF model, we evaluate the Fisher matrix using full-shape information and then add the Fisher matrix corresponding to the difference between the reconstructed and non-reconstructed BAO information in linear theory. While it is feasible to model reconstruction by increasing the amplitude of the BAO information isolated from the DF model, we believe the procedure is more robust and has been more thoroughly explored in linear theory. A more detailed examination of BAO information isolated from nonlinear models is left for future work.

4.4 Optimal modeling and analysis

Table 2 summarizes the different approaches we consider for extracting information from clustering measurements in redshift space. For convenience, these models are numbered 1-6 and are subsequently referred to by number. We consider a BAO-only analysis, with and without reconstruction (models 1 and 2, respectively). We consider three possible approaches to including broadband information. In models 3 (no reconstruction) and 4 (with reconstruction), we use the distribution function model without the correction term to account for deviations at high k_{\parallel} (discussed in Section 3.4), corresponding to $a_4 = 0$ in Equation 3.3. Model 5 employs the same DF model (including reconstruction) but applies a μ -dependent cut in k to remove modes at high k_{\parallel} , where nonlinear redshift-space distortions are particularly challenging to model. In this work, we use the cut denoted by the dotted line in Figure 6 (analyzing only modes below the line). A reasonably straightforward cut can remove the most problematic modes. Although this cut was selected by eye, more sophisticated cut selection is feasible. In model 6, we use the DF model (with reconstruction) and apply the a_4 correction.

Compared to models 3 and 4, models 5 and 6 should reduce the systematic bias introduced by broadband model inaccuracy, although in some specific cases the model can yield different behavior. However, this improvement comes at the cost of statistical constraining power: in model 5 modes are explicitly removed, while model 6 requires simultaneously solving for an additional parameter that is partially degenerate with the parameters of interest. Since these methods predominantly remove information from modes along the line-of-sight,

Model	BAO recon.	Broadband	μ cut	a_4
1	no	no	no	N/A
2	standard	no	no	N/A
3	no	DF	no	0
4	standard	DF	no	0
5	standard	DF	yes	0
6	standard	DF	no	best fit

Table 2. The different models considered in this work are outlined. For convenience, results for each model refer to the labels defined here. See text for descriptions of these model choices.

constraints on H are affected more than those on D_A . In model 6, if strong priors could be placed on a_4 (e.g. from simulations), this loss of statistical power could be mitigated.

In principle, techniques like those in models 5 and 6 will allow an accurate fit to observations on smaller scales. The resulting trade-off between the loss of modes at a given k and a higher unbiased k_{max} must be considered for different scenarios. We note, however, that the forecast assumes a Gaussian covariance matrix, which will no longer hold on sufficiently small scales. The effect of non-Gaussianity is to reduce the information content of additional modes. As a result, approaches that improve the model fit on smaller scales are less powerful than the nominal predictions would indicate. Given similar forecasts for unbiased parameter constraints, a less complex model or analysis technique, with a correspondingly lower k_{max} , is likely preferred.

5 Forecast results

We forecast statistical constraints and systematic biases for parameters of interest as a function of maximum wavenumber (minimum scale) k_{max} . We assume a survey similar to the LRG portion of the proposed DESI experiment, with a volume of $10.5 (h^{-1}\text{Gpc})^3$, corresponding to $0.3 < z < 0.8$, and number density $\bar{n} = 3 \times 10^{-4} (h^{-1}\text{Mpc})^{-3}$. Due to finite simulation snapshots, we focus on results at $z = 0.5$, although this is somewhat lower than the effective redshift of the DESI LRG targets. We show results for halos with biases corresponding to the two lowest mass bins: $b_1 = 1.64$ and 2.18 , respectively, at $z = 0.5$ (see Table 1). Note that the expected LRG bias at this redshift is $b_1 \approx 2.2$. These results are not intended to provide an exact forecast for the DESI experiment, but rather to demonstrate the potential for improvement and challenges for this type of next-generation redshift survey. Constraints scale trivially as $V_s^{1/2}$, with a more complicated scaling with number density, due to the changing relative importance of shot noise. The effect of changing the galaxy bias is more complicated, since both the total signal-to-noise and the relative importance of redshift-space distortions are altered. These effects are discussed below. Since the number density and bias considered here are similar to the CMASS sample in BOSS (e.g. [8, 21]), it is straightforward to compare constraints from each. The approximate volume of the CMASS sample for the completed BOSS survey is $V_s \approx 3.5 (h^{-1}\text{Gpc})^3$, yielding parameter uncertainties larger than those shown here by a factor $\sim (10.5/3.5)^{1/2} = 1.7$. Results from intermediate data releases are additionally increased by $f_{\text{complete}}^{-1/2}$. The true $\bar{n}(z)$ for the CMASS sample is not constant, dropping below $3 \times 10^{-4} (h^{-1}\text{Mpc})^{-3}$ at higher z , which yields a smaller effective volume and further degrades the constraints.

Model	$\sigma[\ln D_A(z)]$ [%] $k_{\max} = (0.10, 0.15, 0.20, 0.25) [h \text{ Mpc}^{-1}]$	$\sigma[\ln H(z)]$ [%]	$\sigma[\ln f\sigma_8(z)]$ [%] (free geometry)	$\sigma[\ln f\sigma_8(z)]$ [%] (fixed geometry)
$b_1 = 1.6$				
1	1.0	2.1	-	-
2	0.6	1.0	-	-
3	0.8, 0.8, 0.7, 0.7	1.5, 1.2 , 0.9, 0.8	3.7, 2.9 , 2.4, 2.0	2.2, 1.3 , 1.0, 0.7
4	0.6, 0.5, 0.5, 0.5	0.9, 0.8 , 0.7, 0.6	3.0, 2.4 , 2.0, 1.7	2.2, 1.3 , 1.0, 0.7
5	0.6, 0.5, 0.5, 0.5	0.9, 0.8, 0.8 , 0.8	3.0, 2.4, 2.2, 2.1	2.2, 1.4, 1.2, 1.2
6	0.6, 0.5, 0.5, 0.5	1.0, 0.9, 0.8 , 0.7	3.3, 2.4, 2.1 , 1.9	2.2, 1.3, 1.0 , 0.7
$b_1 = 2.2$				
1	0.8	1.9	-	-
2	0.5	0.9	-	-
3	0.7, 0.7, 0.7, 0.7	1.4, 1.2, 1.0, 0.9	4.6, 3.7 , 3.0, 2.6	2.6, 1.6 , 1.1, 0.8
4	0.5, 0.5, 0.5, 0.4	0.8, 0.8, 0.7, 0.7	3.5, 2.8 , 2.3, 2.1	2.6, 1.6 , 1.1, 0.8
5	0.5, 0.5, 0.5, 0.5	0.8, 0.8, 0.8, 0.8	3.5, 2.8, 2.4, 2.3	2.6, 1.6, 1.4, 1.3
6	0.5, 0.5, 0.5, 0.5	0.9, 0.8, 0.7, 0.7	3.9, 2.8, 2.4 , 2.1	2.7, 1.5, 1.1 , 0.8

Table 3. Parameter constraints are shown for each model at different values of k_{\max} for $b_1 = 1.6$ (*top*) and $b_1 = 2.2$ (*bottom*) halos at $z = 0.5$. See Table 2 for description of models. Assumed survey corresponds to DESI LRGs. Bold numbers indicate the approximate k_{\max} that minimizes statistical uncertainty without introducing systematic bias at greater than 1σ . To avoid relying on optimistic assumptions on small scales, k_{\max} is chosen to not exceed $0.25h \text{ Mpc}^{-1}$. Here, the choice of k_{\max} affects only broadband information; all BAO information is included. BAO-only provides no constraints on $f\sigma_8$. Constraints on H and D_A involve marginalization over all relevant parameters, including σ_8 . Constraints on $f\sigma_8$ are shown with σ_8 fixed and for both free and fixed geometry; both cases use the applicable k_{\max} for free geometry. See discussion in Section 5.2.

Figures 7-12 show the forecast parameter constraints and systematic biases. Constraints on relevant parameters as a function of k_{\max} , including the approximate best (unbiased) constraints, are given in Table 3.

5.1 Constraints on geometry

Forecasts for measurements of the geometric parameters H and D_A , including both statistical precision and systematic bias, are shown in Figures 7-9. As expected, anisotropic BAO-only information is able to constrain geometry without introducing an appreciable systematic bias into the parameter results. Applying BAO reconstruction significantly improves the resulting constraints (by $\sim 50\%$ for H and $\sim 40\%$ for D_A). These results are consistent with previous forecasts for anisotropic BAO information (e.g. [8, 60]). Reconstruction provides a larger fractional improvement to constraints on H than to those for D_A because of the additional factor of $(1 + f)$ suppressing the BAO in modes along the line-of-sight, which primarily contain information on H .

Including broadband information also improves parameter constraints. For H , including broadband information in the DF model without BAO reconstruction improves constraints by roughly the same amount as reconstruction would have in the BAO-only case ($\sim 50\%$). With reconstruction, including broadband information provides an additional $\sim 30\%$ improvement. The improvement on D_A is somewhat more modest, $\sim 20\%$ and $\sim 30\%$ with and without reconstruction, respectively. The reason for this disparity is discussed below in Section 6. The

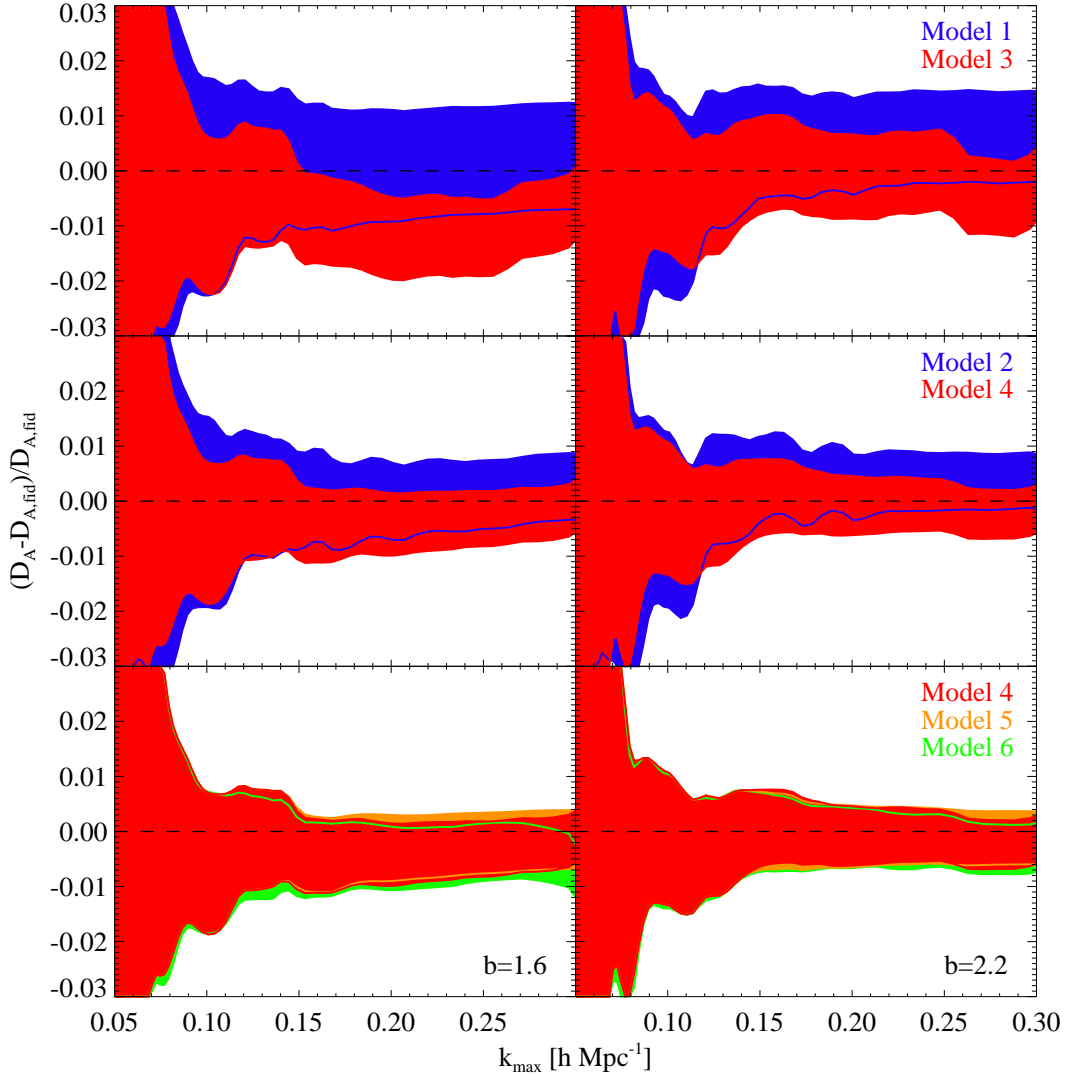


Figure 7. Forecast for recovered $D_A(z)$ value and its statistical uncertainty (1σ), compared with the fiducial value, as a function of k_{\max} for $b_1 = 1.6$ and 2.2 halos at $z = 0.5$. No information from BAO or broadband is included above the given k_{\max} . Assumed survey corresponds to DESI LRGs. *Top panels:* Information from BAO-only (model 1; blue) is compared with full-shape information from the distribution function model (model 3; red). *Middle panels:* Same as top, but standard BAO reconstruction is included: model 2 (blue); model 4 (red). *Bottom panels:* Full shape information is compared for three different cases: model 4 (red); model 5 (yellow); model 6 (green). See Table 2 for description of models.

improvement from including broadband information depends strongly on the k_{\max} to which the model can be reliably used. In the sample-variance limited regime ($\bar{n}P \gg 1$), the square of the total signal-to-noise, corresponding to the amplitude of the Fisher matrix, should scale as the total number of modes ($\sim k_{\max}^3$), with corresponding parameter uncertainties decreasing as $\sigma \sim k_{\max}^{-3/2}$. In the shot-noise-dominated regime ($\bar{n}P \ll 1$), the additional information from

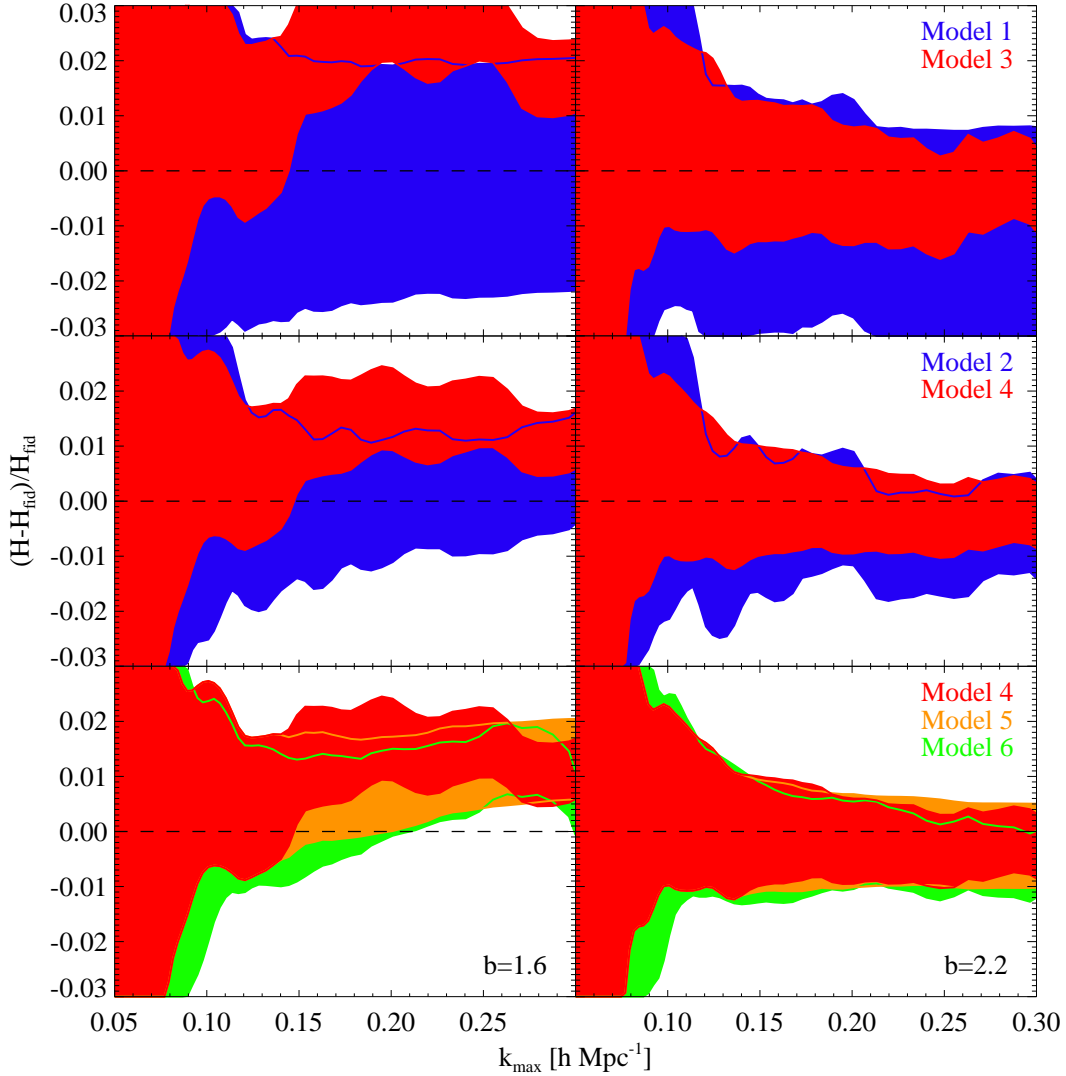


Figure 8. Same as Figure 7, for $H(z)$.

including smaller scales decreases, with rapid saturation in the case of a steeply decreasing $P(k)$ (e.g. the linear theory prediction of $P(k) \propto k^{-3}$ on small scales). Nonlinear evolution yields an excess of power above linear theory, which both delays the onset of the shot-noise-dominated regime and slows the saturation of information once there. For $0.2 \lesssim k_{\max} \lesssim 0.3 h \text{ Mpc}^{-1}$, we find that nonlinear evolution leads to the Fisher matrix amplitude increasing roughly as k_{\max} , with parameter uncertainties thus decreasing as $\sigma \sim k_{\max}^{-1/2}$. The results for models 4-6, seen in Figure 9, demonstrate this qualitative behavior. These approximate scalings are complicated by changing parameter degeneracies or a μ -dependent k cut.

For $b_1 = 1.6$ tracers, systematic bias becomes an issue at $k_{\max} \approx 0.15 h \text{ Mpc}^{-1}$. In the case of $b_1 = 2.2$ tracers, the model is sufficiently accurate to avoid systematic bias of the results on scales as small as $k_{\max} = 0.3 h \text{ Mpc}^{-1}$. However, as previously noted, part of

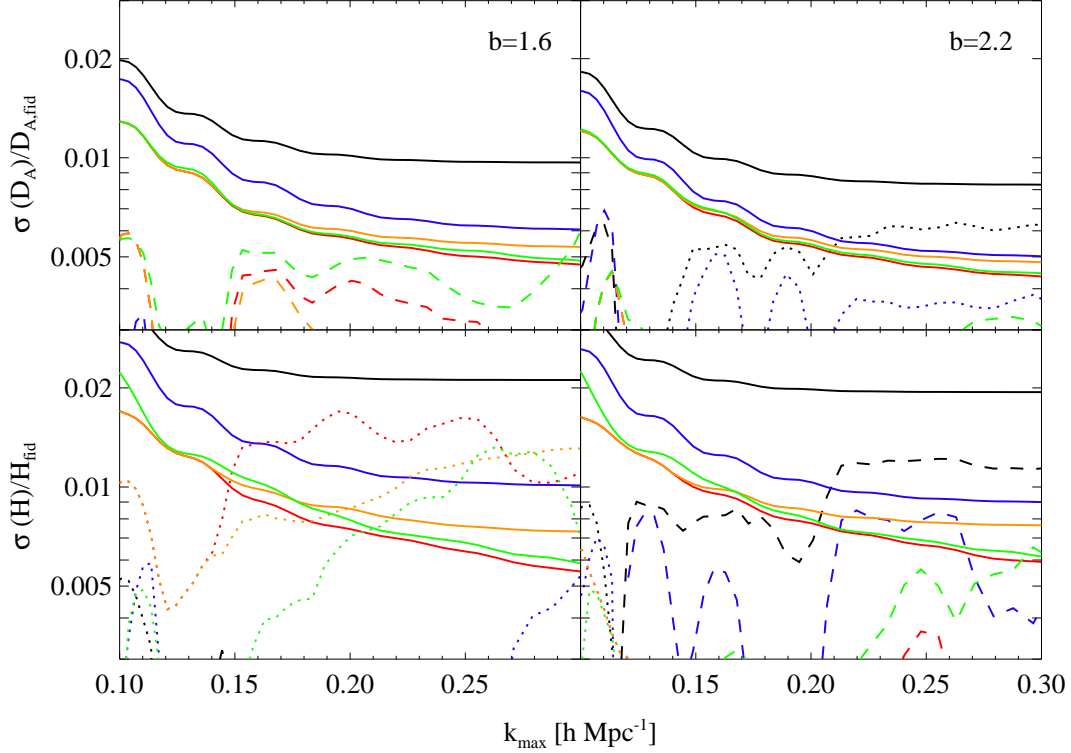


Figure 9. Statistical precision (solid lines) and systematic bias on fractional measurements of D_A (top panels) and H (bottom panels) for $b_1 = 1.6$ and $b_1 = 2.2$ halos at $z = 0.5$. Assumed survey corresponds to DESI LRGs. Positive (negative) systematic bias is indicated with dotted (dashed) lines. Model 1 (black); model 2 (blue); model 4 (red); model 5 (yellow); model 6 (green).

this strong agreement is due to optimistic assumptions regarding the ability to model non-linear biasing and non-Poissonian shot noise. We thus don't consider broadband information beyond $k_{\text{max}} = 0.25h \text{ Mpc}^{-1}$.

Although the survey parameters used here (including redshift, volume, and number density) are chosen to approximate the LRG sample in DESI, it is instructive to compare the performance of halos with different bias, with all other parameters held fixed. In a simple model for $P(k, \mu)$, such as linear theory, low bias tracers provide a more powerful probe of $f\sigma_8$, as discussed below. Because of the strong degeneracy between H and $f\sigma_8$ (both affect line-of-sight modes), one would expect low bias tracers to provide better constraints on H in the sample-variance regime. Indeed, forecasts for linear theory show this behavior, with the lower bias tracers outperforming higher bias tracers on H until shot noise dominates, while for D_A , the higher bias tracers always provide tighter constraints. In the DF model, where nonlinear effects alter the signals and degeneracies for different parameters, these trends are not as clear. As seen in Figure 6, the DF model provides a somewhat better fit for the $b_1 = 2.2$ halos, resulting in reduced systematic parameter biases. To illustrate the degeneracies between parameters, Figures 10 and 11 show joint statistical constraints (without systematic bias) in the $H - D_A$, $H - f\sigma_8$, and $f\sigma_8 - b_1\sigma_8$ planes.

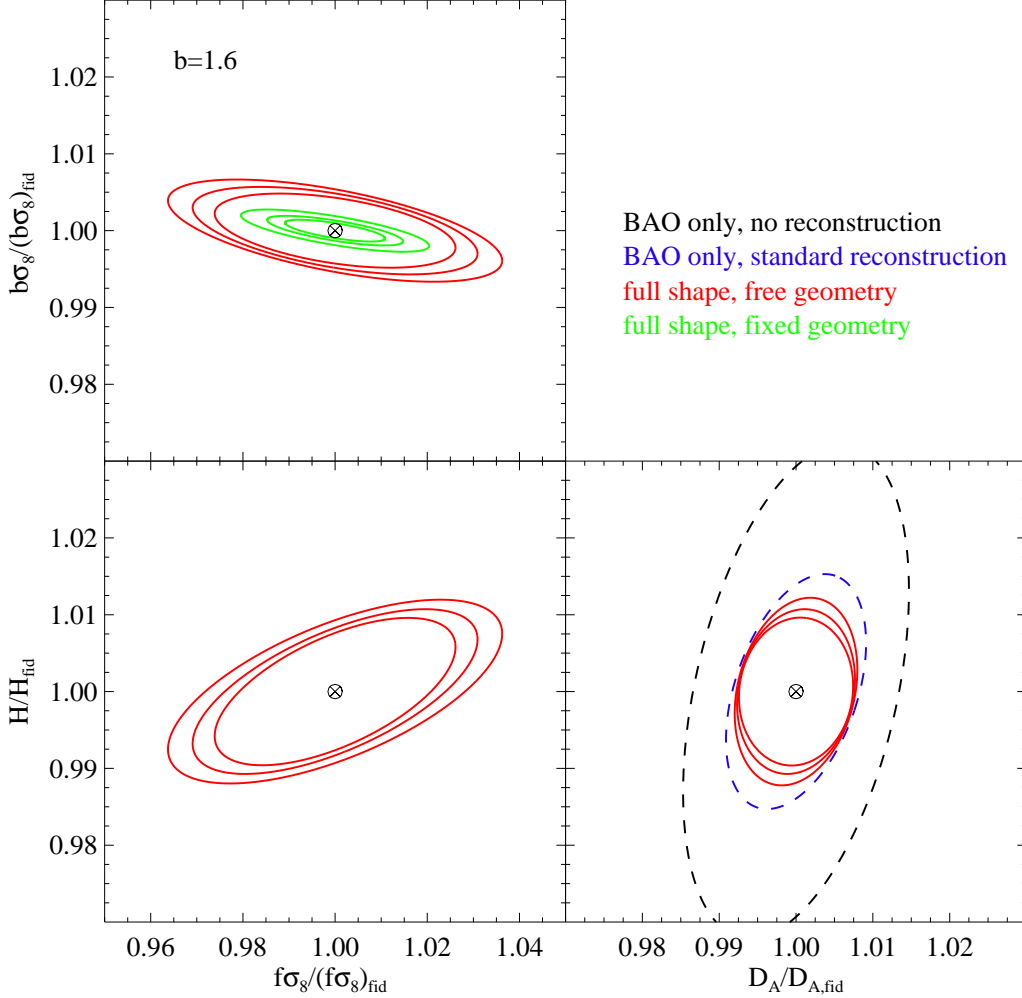


Figure 10. Forecasts for 68% joint statistical uncertainty regions are shown for $b_1 = 1.6$ halos at $z = 0.5$. Assumed survey corresponds to DESI LRGs. Systematic parameter bias is ignored. Red and green solid lines indicate full-shape information has been used (model 4), with green lines indicating that geometry is held fixed. Decreasing contour sizes indicate broadband information is included up to $k_{\text{max}} = \{0.15, 0.20, 0.25\}$. Dashed lines in the $H - D_A$ plane indicate BAO-only information: model 1 (black); model 2 (blue). In all cases, all BAO information is included. As discussed in the text, σ_8 is held fixed for determining constraints on $f\sigma_8$ and $b\sigma_8$. Due to this method, constraints on H differ slightly in the $f\sigma_8 - H$ and $D_A - H$ planes.

The geometric signal coming from ΔV , which changes the overall normalization of $P(k, \mu)$, is in principle quite large. However, in the case of linear theory, this effect is completely degenerate with σ_8 . In the distribution function model, ΔV is not completely degenerate with the parameter set $\{b_1, f, \sigma_8\}$, and thus it results in a modest change to forecast parameter constraints. The effect of ΔV is larger for higher bias objects, where nonlinear

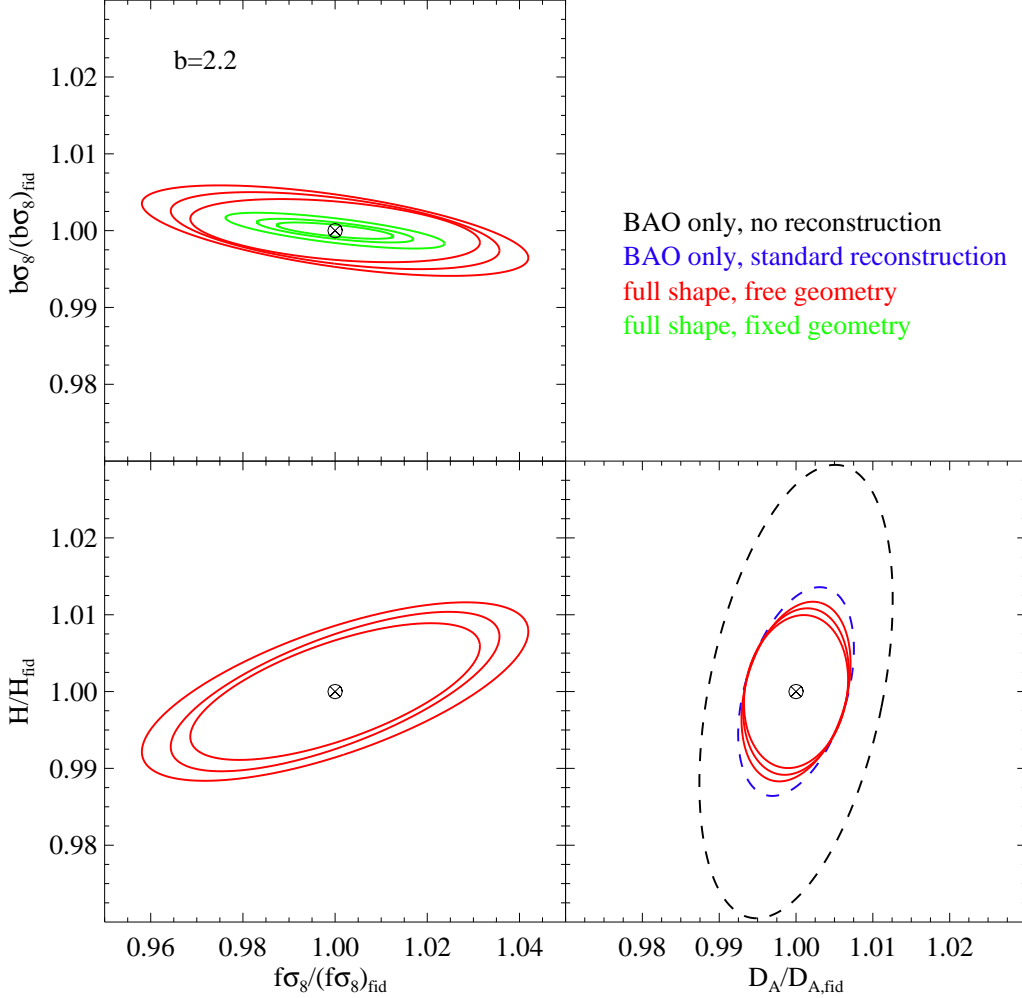


Figure 11. Same as Figure 10, for $b_1 = 2.2$ halos.

contributions to bias and matter clustering result in less degeneracy between $\{b_1, f, \sigma_8\}$ and ΔV .

Forecasts for H and D_A that include broadband information marginalize over σ_8 in addition to b_1 and f . Because σ_8 is largely degenerate with the other two (in combination), the additional marginalization has little impact on statistical uncertainties. However, because there is not total degeneracy between these parameters, holding σ_8 fixed can lead to a systematic bias in H and D_A , since the modeling error can lead to a change in the preferred value of H and D_A . The size and direction of this effect depends on the particular halo mass bin and minimum scale being considered.

Finally, the two more sophisticated analysis techniques explored here - applying a μ -dependent cut in k (model 5) and fitting an additional parameter to correct for higher μ

dependence (model 6), do not yield improved overall constraints. The loss in statistical information is not sufficiently offset by a reduction in systematic bias.

5.2 Constraints on growth of structure

Figures 10 and 11 show the forecast measurement precision for $f\sigma_8$ and $b_1\sigma_8$, using full shape information in the DF model. Figure 12 shows both statistical precision and systematic bias for measurements of $f\sigma_8$ (or f , if σ_8 is simultaneously measured) using different versions of the DF model. While the linear theory $P(k, \mu)$ depends only on $f\sigma_8$ and $b_1\sigma_8$, the distribution function model has nonlinear contributions that scale with additional powers of σ_8 , and nonlinear bias provides nontrivial dependence on b_1 , thus breaking this degeneracy. As seen in Figure 12, this breaking occurs on small scales. In these figures (unless otherwise noted), constraints on $\{f\sigma_8, b_1\sigma_8\}$ are actually constraints on $\{f, b_1\}$, with σ_8 held fixed. In the limit where the σ_8 dependence appears only in $f\sigma_8$ and $b_1\sigma_8$ (e.g. in linear theory or on large scales in the DF model), these approaches are equivalent. As this degeneracy is broken, the two are no longer the same. However, the degeneracy is sufficient on the scales considered here that the deviation remains small. Despite differences in model and technique, we find constraints on $f\sigma_8$ (fixed geometry) that are consistent with the recent results of [8].

As is apparent in Figures 10-12, the degeneracy between geometry and growth of structure is quite strong. Indeed, at leading order, geometric and redshift-space distortions have the same effect on the power spectrum, introducing a μ^2 dependence. Thus, strong priors on either geometry or growth of structure will allow significantly improved constraints on the other. Since linear redshift-space distortions have an amplitude characterized by $\beta \equiv f/b_1$, lower bias tracers provide a higher signal-to-noise measurement of RSD. Moreover, when trying to simultaneously constrain growth rate and geometry, higher β reduces the degeneracy between RSD and geometric distortions by increasing the relative importance of higher μ -dependence. These advantages are diminished at high k , where shot noise becomes significant. Similarly, although the BAO alone provides no constraints on $f\sigma_8$, it improves constraints when combined with broadband information because it is able to separately measure H and D_A , breaking the degeneracy with $f\sigma_8$. In this case, reconstruction further improves constraints.

Also of interest is the potential benefit of a more sophisticated model (using the a_4 correction) or analysis technique (applying a μ -dependent cut in k). While these techniques seem to provide little advantage for geometric constraints, they can significantly improve the precision of an unbiased measurement of $f\sigma_8$ by allowing the inclusion of information at higher k (see the middle and bottom panels of Figure 12). The improvement may be even more significant in the case where prior measurements allow geometry and/or bias to be held fixed. As is clear in the top panels of Figure 12, the systematic bias on $f\sigma_8$ is largely unaffected by whether or not geometry and bias are held fixed. Thus, even if separate measurements of geometry or bias existed, the uncorrected DF model lacks sufficient broadband accuracy to take advantage of the improved statistical precision. Note that the $f\sigma_8$ constraints shown in Table 3 for both free and fixed geometry use the optimal k_{max} determined for free geometry.

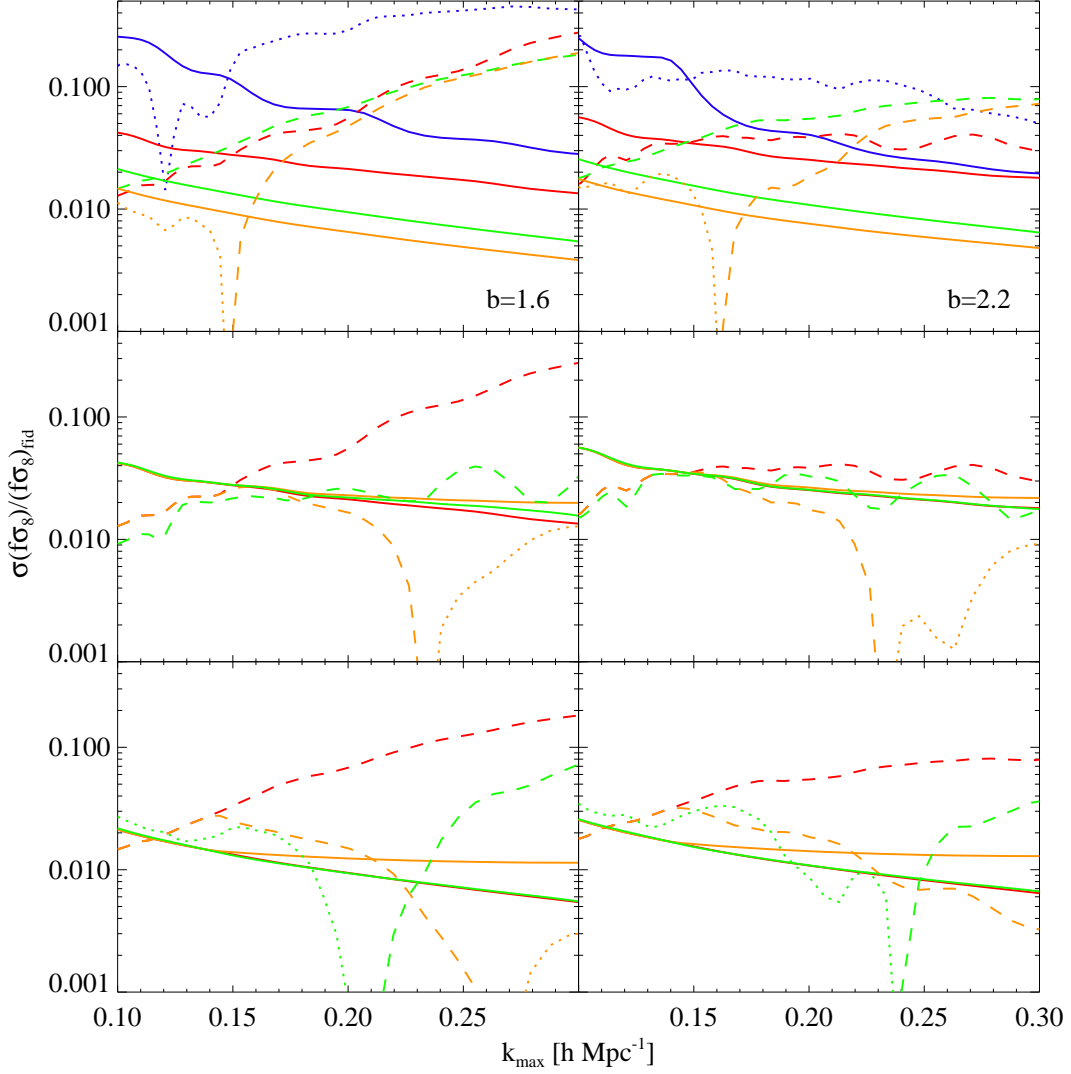


Figure 12. Statistical precision (solid lines) and systematic bias on $f\sigma_8$ for $b_1 = 1.6$ and $b_1 = 2.2$ halos at $z = 0.5$. Assumed survey corresponds to DESI LRGs. Positive (negative) systematic bias is indicated with dotted (dashed) lines. *Top panels:* The effect of allowing different parameters to vary in model 4 is shown. Blue line shows fractional precision and bias on f alone (all other parameters, including σ_8 , are allowed to vary). With σ_8 held fixed, thus leading to constraints on $f\sigma_8$: bias and geometry are allowed to vary (red); geometry is fixed (green); both bias and geometry are fixed (yellow). *Middle panels:* Constraints on $f\sigma_8$ (σ_8 held fixed; geometry and bias free) are shown for model 4 (red); model 5 (yellow); model 6 (green). *Bottom panels:* Same as middle panels, but with σ_8 and geometry held fixed; bias free.

6 Discussion

The results in this work show the potential advantages of analyzing the broadband shape of $P(k, \mu)$, in addition to the BAO feature, when a sufficiently accurate model is used. Including broadband information when using linear theory provides little gain: the systematic bias due to the inaccuracy of the model quickly overwhelms the statistical gain. Similar results have been seen in previous studies examining measurements of f from broadband information (e.g. [33]), where model inaccuracy results in systematically biased parameter constraints on relatively large scales. As shown here, the situation can be significantly improved when using a more accurate model, such as the distribution function model of [14]. Applying this model, we demonstrate the potential for precision geometric measurements using broadband information, as well as improved constraints on growth of structure from measuring redshift-space distortions at smaller scales.

Including broadband information improves constraints on H more significantly than those on D_A . This disparity is due to the different geometric degeneracies in BAO and broadband measurements. While the BAO feature is able to measure H and D_A separately, the primary signal is in the position of the angle-averaged BAO position, which measures (roughly) the parameter combination D_A^2/H . Thus, constraints are stronger on D_A . Equivalently, we can see that since there are more transverse modes than line-sight-modes, measurements of a transverse distance scale will be more precise. While similar arguments hold for any features in the broadband shape, the bulk of broadband information is coming from the Alcock-Paczynski test, which carries signal even in the absence of features at a known scale. Since this test is measuring $D_A H$ (the “warping” mode), it serves to break the degeneracy remaining in the BAO-only information, primarily benefiting the previously poorer constraints on H .

Although there are differences in the models and techniques applied, our results are broadly consistent with other recent Fisher forecasts (e.g. [8, 60]). However, in some cases, recent measurements on real or mock data sets have yielded less precise constraints (e.g. [21]). While some of this disparity may be due to the inherently optimistic nature of Fisher forecasts (they provide a lower limit on statistical uncertainty), there may be other effects contributing as well, such as survey geometry.

Our results indicate the potential value of adding external measurements able to break degeneracies between geometry, growth of structure, and bias. For instance, constraints on $f\sigma_8$ are significantly improved if geometry is already known. Similarly, the effect of the geometric factor ΔV is to cause an overall rescaling of the power spectrum amplitude. This effect is largely degenerate with b_1 and σ_8 , even when nonlinear corrections are included. However, if these parameters can be measured separately, the signal-to-noise for measuring ΔV (and thus constraining D_V) is very high.

We also highlight advantages of low bias tracers, which have a higher signal-to-noise for measuring RSD. Alternatively, tracers with an additional velocity bias that increases the relative strength of RSD will exhibit similar advantages. Although an unknown velocity bias would be degenerate with measurements of f (in the absence of accurate modeling), it is easier to measure broadband geometric distortions in the presence of stronger RSD, which are less degenerate, especially with H . These arguments suggest that performing an AP test with anisotropic Lyman- α clustering is an interesting possibility.

As described in Section 3.3, our construction of a distribution function model for halo clustering in redshift space is somewhat optimistic. However, given the recent progress in

understanding halo biasing and stochasticity, as well as improvements in analytic and numerical approaches at rapidly estimating the dark matter power spectrum for a given cosmology (including improved perturbative techniques and cosmological emulators based on suites of simulations), some of the complications in constructing an accurate model are diminishing. The step from describing dark matter halos to the luminous galaxies that are actually observed introduces the additional challenge of incorporating the complexity of galaxy behavior, including satellite objects and virial motions within halos. The use of multiple, overlapping tracers to reduce sample variance (e.g. [62, 63]) can in some circumstances improve constraints. These issues are the subject of ongoing and future work. Finally, we note that these considerations are not limited to galaxy redshift surveys, but can also apply to any three-dimensional tracer of the density field, including neutral hydrogen seen in the Lyman- α forest and the 21cm line.

Acknowledgments

We thank Beth Reid, Hee-Jong Seo, Florian Beutler, Chris Hirata, and David Weinberg for useful discussions. J.B. appreciates the hospitality of the Institute for Theoretical Physics at the University of Zurich, where part of this work was done. This work is supported by the DOE, the Swiss National Foundation under contract 200021-116696/1, WCU grant R32-10130, and Ewha University research fund 1-2008-2935-001-2.

References

- [1] D. J. Eisenstein and W. Hu, *Baryonic Features in the Matter Transfer Function*, ApJ **496** (Mar., 1998) 605, [[astro-ph/9709112](#)].
- [2] M. Tegmark *et. al.*, *The Three-Dimensional Power Spectrum of Galaxies from the Sloan Digital Sky Survey*, ApJ **606** (May, 2004) 702–740, [[astro-ph/0310725](#)].
- [3] J. Lesgourgues and S. Pastor, *Massive neutrinos and cosmology*, Phys. Rep. **429** (July, 2006) 307–379, [[astro-ph/0603494](#)].
- [4] N. Dalal, O. Doré, D. Huterer, and A. Shirokov, *Imprints of primordial non-Gaussianities on large-scale structure: Scale-dependent bias and abundance of virialized objects*, Phys.Rev.D **77** (June, 2008) 123514, [[arXiv:0710.4560](#)].
- [5] C. Alcock and B. Paczynski, *An evolution free test for non-zero cosmological constant*, Nature **281** (Oct., 1979) 358.
- [6] D. J. Eisenstein, H.-J. Seo, and M. White, *On the Robustness of the Acoustic Scale in the Low-Redshift Clustering of Matter*, ApJ **664** (Aug., 2007) 660–674, [[astro-ph/0604361](#)].
- [7] E. Jennings, C. M. Baugh, and S. Pascoli, *Testing Gravity Using the Growth of Large-scale Structure in the Universe*, ApJL **727** (Jan., 2011) L9, [[arXiv:1011.2842](#)].
- [8] A. Font-Ribera, P. McDonald, N. Mostek, B. A. Reid, H.-J. Seo, and A. Slosar, *DESI and other dark energy experiments in the era of neutrino mass measurements*, ArXiv e-prints (Aug., 2013) [[arXiv:1308.4164](#)].
- [9] N. Kaiser, *Clustering in real space and in redshift space*, MNRAS **227** (July, 1987) 1–21.
- [10] R. Scoccimarro, *Redshift-space distortions, pairwise velocities, and nonlinearities*, Phys.Rev.D **70** (Oct., 2004) 083007, [[astro-ph/0407214](#)].
- [11] A. Taruya, T. Nishimichi, and S. Saito, *Baryon acoustic oscillations in 2D: Modeling redshift-space power spectrum from perturbation theory*, Phys.Rev.D **82** (Sept., 2010) 063522, [[arXiv:1006.0699](#)].

- [12] U. Seljak and P. McDonald, *Distribution function approach to redshift space distortions*, JCAP **11** (Nov., 2011) 39, [[arXiv:1109.1888](#)].
- [13] Z. Vlah, U. Seljak, P. McDonald, T. Okumura, and T. Baldauf, *Distribution function approach to redshift space distortions. Part IV: perturbation theory applied to dark matter*, ArXiv e-prints (July, 2012) [[arXiv:1207.0839](#)].
- [14] Z. Vlah, U. Seljak, T. Okumura, and V. Desjacques, *Distribution function approach to redshift space distortions. Part V: perturbation theory applied to dark matter halos*, ArXiv e-prints (Aug., 2013) [[arXiv:1308.6294](#)].
- [15] T. Okumura, U. Seljak, and V. Desjacques, *Distribution function approach to redshift space distortions. Part III: halos and galaxies*, JCAP **11** (Nov., 2012) 14, [[arXiv:1206.4070](#)].
- [16] T. Okumura, U. Seljak, P. McDonald, and V. Desjacques, *Distribution function approach to redshift space distortions. Part II: N-body simulations*, JCAP **2** (Feb., 2012) 10, [[arXiv:1109.1609](#)].
- [17] A. Vallinotto and E. V. Linder, *Redshift Space Distortion Reconstruction*, ArXiv e-prints (July, 2013) [[arXiv:1307.2906](#)].
- [18] D. J. Eisenstein *et. al.*, *Detection of the Baryon Acoustic Peak in the Large-Scale Correlation Function of SDSS Luminous Red Galaxies*, ApJ **633** (Nov., 2005) 560–574, [[astro-ph/0501171](#)].
- [19] W. J. Percival *et. al.*, *Baryon acoustic oscillations in the Sloan Digital Sky Survey Data Release 7 galaxy sample*, MNRAS **401** (Feb., 2010) 2148–2168, [[arXiv:0907.1660](#)].
- [20] C. Blake *et. al.*, *The WiggleZ Dark Energy Survey: mapping the distance-redshift relation with baryon acoustic oscillations*, MNRAS **418** (Dec., 2011) 1707–1724, [[arXiv:1108.2635](#)].
- [21] L. Anderson *et. al.*, *The clustering of galaxies in the SDSS-III Baryon Oscillation Spectroscopic Survey: Baryon Acoustic Oscillations in the Data Release 9 Spectroscopic Galaxy Sample*, ArXiv e-prints (Mar., 2012) [[arXiv:1203.6594](#)].
- [22] T. Okumura, T. Matsubara, D. J. Eisenstein, I. Kayo, C. Hikage, A. S. Szalay, and D. P. Schneider, *Large-Scale Anisotropic Correlation Function of SDSS Luminous Red Galaxies*, ApJ **676** (Apr., 2008) 889–898, [[arXiv:0711.3640](#)].
- [23] C. Blake *et. al.*, *The WiggleZ Dark Energy Survey: measuring the cosmic expansion history using the Alcock-Paczynski test and distant supernovae*, MNRAS **418** (Dec., 2011) 1725–1735, [[arXiv:1108.2637](#)].
- [24] B. A. Reid *et. al.*, *The clustering of galaxies in the SDSS-III Baryon Oscillation Spectroscopic Survey: measurements of the growth of structure and expansion rate at $z = 0.57$ from anisotropic clustering*, MNRAS **426** (Nov., 2012) 2719–2737, [[arXiv:1203.6641](#)].
- [25] L. Anderson *et. al.*, *The clustering of galaxies in the SDSS-III Baryon Oscillation Spectroscopic Survey: Measuring D_A and H at $z=0.57$ from the Baryon Acoustic Peak in the Data Release 9 Spectroscopic Galaxy Sample*, ArXiv e-prints (Mar., 2013) [[arXiv:1303.4666](#)].
- [26] E. A. Kazin *et. al.*, *The Clustering of Galaxies in the SDSS-III Baryon Oscillation Spectroscopic Survey: Measuring $H(z)$ and $D_A(z)$ at $z = 0.57$ with Clustering Wedges*, ArXiv e-prints (Mar., 2013) [[arXiv:1303.4391](#)].
- [27] A. G. Sánchez *et. al.*, *The clustering of galaxies in the SDSS-III Baryon Oscillation Spectroscopic Survey: cosmological constraints from the full shape of the clustering wedges*, MNRAS **433** (Aug., 2013) 1202–1222, [[arXiv:1303.4396](#)].
- [28] F. Beutler *et. al.*, in preparation.
- [29] M. Levi *et. al.*, *The DESI Experiment, a whitepaper for Snowmass 2013*, ArXiv e-prints (Aug., 2013) [[arXiv:1308.0847](#)].

- [30] W. E. Ballinger, J. A. Peacock, and A. F. Heavens, *Measuring the cosmological constant with redshift surveys*, MNRAS **282** (Oct., 1996) 877, [[astro-ph/9605017](#)].
- [31] N. Padmanabhan and M. White, *Constraining anisotropic baryon oscillations*, Phys.Rev.D **77** (June, 2008) 123540, [[arXiv:0804.0799](#)].
- [32] F. Montanari and R. Durrer, *New method for the Alcock-Paczynski test*, Phys.Rev.D **86** (Sept., 2012) 063503, [[arXiv:1206.3545](#)].
- [33] J. Kwan, G. F. Lewis, and E. V. Linder, *Mapping Growth and Gravity with Robust Redshift Space Distortions*, ApJ **748** (Apr., 2012) 78, [[arXiv:1105.1194](#)].
- [34] E. V. Linder and J. Samsing, *Power spectrum precision for redshift space distortions*, JCAP **2** (Feb., 2013) 25, [[arXiv:1211.2274](#)].
- [35] M. Shoji, D. Jeong, and E. Komatsu, *Extracting Angular Diameter Distance and Expansion Rate of the Universe From Two-Dimensional Galaxy Power Spectrum at High Redshifts: Baryon Acoustic Oscillation Fitting Versus Full Modeling*, ApJ **693** (Mar., 2009) 1404–1416, [[arXiv:0805.4238](#)].
- [36] A. Taruya, S. Saito, and T. Nishimichi, *Forecasting the cosmological constraints with anisotropic baryon acoustic oscillations from multipole expansion*, Phys.Rev.D **83** (May, 2011) 103527, [[arXiv:1101.4723](#)].
- [37] E. A. Kazin, A. G. Sánchez, and M. R. Blanton, *Improving measurements of $H(z)$ and $D_A(z)$ by analysing clustering anisotropies*, MNRAS **419** (Feb., 2012) 3223–3243, [[arXiv:1105.2037](#)].
- [38] H. Gil-Marín, C. Wagner, L. Verde, C. Porciani, and R. Jimenez, *Perturbation theory approach for the power spectrum: from dark matter in real space to massive haloes in redshift space*, JCAP **11** (Nov., 2012) 29, [[arXiv:1209.3771](#)].
- [39] Y.-S. Song, T. Okumura, and A. Taruya, *Broadband Alcock-Paczynski test exploiting redshift distortions*, ArXiv e-prints (Sept., 2013) [[arXiv:1309.1162](#)].
- [40] A. Oka, S. Saito, T. Nishimichi, A. Taruya, and K. Yamamoto, *Simultaneous constraints on the growth of structure and cosmic expansion from the multipole power spectra of the SDSS DR7 LRG sample*, ArXiv e-prints (Oct., 2013) [[arXiv:1310.2820](#)].
- [41] E. Jennings, C. M. Baugh, and S. Pascoli, *Modelling redshift space distortions in hierarchical cosmologies*, MNRAS **410** (Jan., 2011) 2081–2094, [[arXiv:1003.4282](#)].
- [42] B. A. Reid and M. White, *Towards an accurate model of the redshift-space clustering of haloes in the quasi-linear regime*, MNRAS **417** (Nov., 2011) 1913–1927, [[arXiv:1105.4165](#)].
- [43] T. Baldauf, U. Seljak, V. Desjacques, and P. McDonald, *Evidence for quadratic tidal tensor bias from the halo bispectrum*, Phys.Rev.D **86** (Oct., 2012) 083540, [[arXiv:1201.4827](#)].
- [44] E. V. Linder, *Cosmic growth history and expansion history*, Phys.Rev.D **72** (Aug., 2005) 043529, [[astro-ph/0507263](#)].
- [45] B. A. Reid and D. N. Spergel, *Constraining the Luminous Red Galaxy Halo Occupation Distribution Using Counts-In-Cylinders*, ApJ **698** (June, 2009) 143–154, [[arXiv:0809.4505](#)].
- [46] T. Nishimichi and A. Oka, *Simulating the Anisotropic Clustering of Luminous Red Galaxies with Subhalos: A Direct Confrontation with Observation and Cosmological Implications*, ArXiv e-prints (Oct., 2013) [[arXiv:1310.2672](#)].
- [47] V. Desjacques, U. Seljak, and I. T. Iliev, *Scale-dependent bias induced by local non-Gaussianity: a comparison to N-body simulations*, MNRAS **396** (June, 2009) 85–96, [[arXiv:0811.2748](#)].
- [48] E. Komatsu et. al., *Five-Year Wilkinson Microwave Anisotropy Probe Observations: Cosmological Interpretation*, ApJS **180** (Feb., 2009) 330–376, [[arXiv:0803.0547](#)].
- [49] M. Davis, G. Efstathiou, C. S. Frenk, and S. D. M. White, *The evolution of large-scale structure in a universe dominated by cold dark matter*, ApJ **292** (May, 1985) 371–394.

- [50] J. Kwan, S. Bhattacharya, K. Heitmann, and S. Habib, *Cosmic Emulation: The Concentration-Mass Relation for w CDM Universes*, ApJ **768** (May, 2013) 123, [[arXiv:1210.1576](#)].
- [51] S. Saito *et. al.*, in preparation.
- [52] K. C. Chan, R. Scoccimarro, and R. K. Sheth, *Gravity and large-scale nonlocal bias*, Phys.Rev.D **85** (Apr., 2012) 083509, [[arXiv:1201.3614](#)].
- [53] T. Baldauf, U. Seljak, R. E. Smith, N. Hamaus, and V. Desjacques, *Halo Stochasticity from Exclusion and non-linear Clustering*, ArXiv e-prints (May, 2013) [[arXiv:1305.2917](#)].
- [54] U. Seljak, N. Hamaus, and V. Desjacques, *How to Suppress the Shot Noise in Galaxy Surveys*, Physical Review Letters **103** (Aug., 2009) 091303, [[arXiv:0904.2963](#)].
- [55] M. Crocce and R. Scoccimarro, *Renormalized cosmological perturbation theory*, Phys.Rev.D **73** (Mar., 2006) 063519, [[astro-ph/0509418](#)].
- [56] M. Pietroni, *Flowing with time: a new approach to non-linear cosmological perturbations*, JCAP **10** (Oct., 2008) 36, [[arXiv:0806.0971](#)].
- [57] A. Taruya, F. Bernardeau, T. Nishimichi, and S. Codis, *Direct and fast calculation of regularized cosmological power spectrum at two-loop order*, Phys.Rev.D **86** (Nov., 2012) 103528, [[arXiv:1208.1191](#)].
- [58] M. Tegmark, *Measuring Cosmological Parameters with Galaxy Surveys*, Physical Review Letters **79** (Nov., 1997) 3806–3809, [[astro-ph/9706198](#)].
- [59] H.-J. Seo and D. J. Eisenstein, *Probing Dark Energy with Baryonic Acoustic Oscillations from Future Large Galaxy Redshift Surveys*, ApJ **598** (Dec., 2003) 720–740, [[astro-ph/0307460](#)].
- [60] H.-J. Seo and D. J. Eisenstein, *Improved Forecasts for the Baryon Acoustic Oscillations and Cosmological Distance Scale*, ApJ **665** (Aug., 2007) 14–24, [[astro-ph/0701079](#)].
- [61] D. J. Eisenstein, H.-J. Seo, E. Sirko, and D. N. Spergel, *Improving Cosmological Distance Measurements by Reconstruction of the Baryon Acoustic Peak*, ApJ **664** (Aug., 2007) 675–679, [[astro-ph/0604362](#)].
- [62] P. McDonald and U. Seljak, *How to evade the sample variance limit on measurements of redshift-space distortions*, JCAP **10** (Oct., 2009) 7, [[arXiv:0810.0323](#)].
- [63] N. Hamaus, U. Seljak, and V. Desjacques, *Optimal weighting in galaxy surveys: Application to redshift-space distortions*, Phys.Rev.D **86** (Nov., 2012) 103513, [[arXiv:1207.1102](#)].